THE ASTROPHYSICAL JOURNAL SUPPLEMENT SERIES, 39:1–27, 1979 January

SHOCK WAVES IN THE INTERSTELLAR MEDIUM

JOHN C. RAYMOND
Space Physics Laboratory, University of Wisconsin
Received 1978 January 16; accepted 1978 June 26

ABSTRACT

Calculations of the optical and UV emission-line intensities and column densities of ions observable in the optical and UV are presented for plane-parallel, steady-state shock waves in the interstellar medium. The range of shock velocities considered is 50 km $s^{-1} \leq v_s \leq 200$ km s^{-1}, and preshock densities are 1 $cm^{-3} \leq n_0 \leq 300$ cm^{-3}. The ionization state of the preshock gas is found to be an important parameter, and several sets of elemental abundances corresponding to various amounts of depletion onto grains are used. The results are compared with observations of the Cygnus Loop, the Vela supernova remnant, and Herbig-Haro objects.

Subject headings: interstellar: matter — nebulae: supernova remnants — shock waves

I. INTRODUCTION

When gas flows into a shock front, some of its flow velocity is converted into random thermal velocity. In the models presented here this conversion takes place in a small distance, causing a sudden jump of temperature and density. Collisional ionization in the hot postshock gas drives the ionization state toward the equilibrium ionization balance for the postshock temperature, but the equilibrium state is not reached, because radiative cooling lowers the temperature. Eventually the gas becomes cooler than the temperature corresponding to its ionization state and begins to recombine. Analysis of the spectral lines emitted in the course of this cooling and recombination can yield information about the shock itself and about the gas into which it is moving.

These models extend the work of Cox (1972*a*, *b*) and Daltabuit (1972) by including several more elements in the calculations, by using more detailed atomic physics in the calculations, and by investigating the dependence of the flow and of the emission spectrum on variables which had previously been held fixed. Photoionization of all ions is now included, and improved rates are used for many atomic processes. The calculational procedure has been improved by starting with the ionization balance of the preshock gas, rather than by assuming ionization equilibrium at the postshock temperature. The present models and those of Dopita (1976, 1977) are mutually complementary in that these treat some aspects of the ionization and recombination in greater detail, while those of Dopita cover a better grid of abundance and velocity assumptions.

The basic assumptions and the methods of calculation of the shock models are described in § II, and the atomic physics pertaining to the emission of radiation and to the ionization state is discussed in § III. Section IV presents the results of the calculations and discusses the dependence of emission spectra on the parameters of the model. Section V outlines the use of the models in interpretation of observed spectra and considers the Cygnus Loop, the Vela supernova remnant, and Herbig-Haro objects in detail.

II. METHODS OF CALCULATION

a) Dynamics

The treatment of the dynamics of the shocked gas is similar to that used by Cox (1972*a*). The flow is taken to be plane parallel and constant in time. With these assumptions, the calculation can be performed by following an element of gas as it flows through the shock, becomes heated and ionized, then cools and recombines. A temporal integration following this element of gas, rather than a spatial one, gives the total emission spectrum due to the shock.

These assumptions were made with the intention of modeling a shock driven by the cold expanding shell of an old supernova remnant, but the models are applicable to other shocks, provided the scale of the flow perpendicular to the flow direction is large compared to the thickness of the cooling region (plane-parallel assumption) and provided the flow parameters remain constant during the time required for gas to cool from the postshock temperature to a temperature low enough that optical emission ceases. It is also assumed that only radiation from the shocked gas and Galactic background starlight are present.

The other important assumptions involve the use of fluid equations to describe the flow, the equality of electron and ion temperatures, and the assumptions that heat conduction and the thickness of the shock front itself are negligible. These assumptions are discussed in detail by Cox (1970) and Raymond (1976) and are found to be justified for shocks in ionized gas up to 200 km s^{-1}. Neglect of thermal conduction in shocks moving nearly parallel to the magnetic field ($\theta < 20°$) introduces some error in the treatment of the immediate postshock region of shocks faster than 100 km s^{-1}, but this should have little effect on predicted line intensities.

With these assumptions, we have a set of flow equations similar to those given by Cox (1972*a*):

$$nv = n_0 v_0 ,$$

$$P + \rho v^2 + \frac{B^2}{8\pi} = n_0\left(1 + \frac{f_0}{a_n}\right)kT_0 + \rho_0 v_s{}^2 + \frac{B_0{}^2}{8\pi} ,$$

$$\frac{dh}{dt} = -Ln_e .$$

The subscript zero refers to preshock conditions, and the density of ions and neutrals is n. The transverse magnetic field $B = (n/n_0)B_0$ is frozen in, f_0 is the initial ionization fraction of hydrogen, and $a_n \approx 1 + n(\mathrm{He})/n(\mathrm{H})$ is the number of atoms per hydrogen atom. The enthalpy per nucleus is

$$h = \epsilon_I + \frac{B^2}{4\pi n} + \frac{\mu v^2}{2} + 2.5\left(1 + \frac{n_e}{n}\right)kT ,$$

with mean ionization energy per nucleus ϵ_I and average nuclear mass μ. The net loss rate Ln_e is the difference between the radiative cooling rate and the rate of heating by photoionization.

Several of the models have partially neutral hydrogen in the preshock gas; because neutrals are not subject to the Coulomb collisions which randomize the bulk velocity of ions and electrons, the neutrals were treated as a separate fluid which interacts with the ionized component through collisions having a cross section $\sim 10^{-16}$ cm^{-2}. While this is reasonable for elastic collisions, it neglects charge exchange, which has a cross section over 10 times larger. The equations for mass, energy, and momentum conservation of each fluid, including ionization and collisional coupling between them, were treated adequately, but the proper charge exchange cross section makes the thickness of the layer in which a two-fluid treatment is needed negligibly thin. The conclusion that H I cooling dominates the initial cooling (Raymond 1976) remains valid; the intensities of Hβ and the forbidden lines will be generally correct, but less accurate than in models of shocks in fully ionized gas. The enhanced Hα intensities given in Raymond (1976) are incorrect.

b) Radiative Transfer

The computer calculations treat only the continuum processes involved in radiative transfer. At each step in the flow the radiation emitted in each of 500 energy bands is calculated. Typically, these bands start at 7 eV and are $\frac{1}{2}$–1 eV wide.

The optical depth between two steps, i and j, for photons in energy bin k is

$$\tau(i, j, k) = N_{ij}(\mathrm{H})\sigma(\mathrm{H}) + N_{ij}(\mathrm{He\ I})\sigma(\mathrm{He\ I}) + N_{ij}(\mathrm{He\ II})\sigma(\mathrm{He\ II}) ,$$

where N_{ij} denotes the column density between steps i and j and the σ's are photoionization cross sections at the energy of bin k.

This gives a photoionization rate for any ion

$$c_{\mathrm{phot}} = \sum_j \sum_k \frac{N_{\mathrm{phot}}(j, k)}{2} \sigma_{\mathrm{ion}}(k) E_1[\tau(i, j, k)] .$$

The number of photons emitted in bin k during step j is $N_{\mathrm{phot}}(j, k)$, and $E_1(\tau)$ is the exponential integral of index 1. In practice, some cutoff must be used, since $E_1(\tau)$ diverges as $\tau \to 0$.

The cutoff of E_1 for small τ is taken to be a free parameter $R_{\max}$ which depends on the ratio of the scale of the shock front perpendicular to the flow direction to the thickness of the postshock region (L/D). Models were run with $R_{\max} = 3.0$, 1.0, and 0.3, which correspond to an infinite plane shock (Shull and McKee 1978), $L/D \approx 5$, and $L/D \approx 2$, respectively.

Resonant scattering of line radiation does not affect the total number of photons and is therefore ignored in the calculations. A few lines are important enough to require further discussion, however.

For H I and He I recombination lines, case B is assumed, which is appropriate since resonance lines of these ions are scattered many times. For the He II 4686 Å line, however, case A is assumed, since the He II resonance lines which affect this line (ground state to $n = 4$ and above) have optical depths less than 5 at line center.

The He II 304 Å resonance line can be quite strong in shocks at about 100 km s^{-1} if the helium in the preshock gas is not doubly ionized. For shocks less than 140 km s^{-1}, the postshock gas is not hot enough to ionize He II quickly but the temperature may be sufficiently high to excite the He II ions many times. The 304 Å line thus produced can account for a large share of the cooling rate and can dominate the photoionization rates of He I, O II, and N II.

Although the 304 Å line is also produced by recombinations of He III, it has important effects on the flow and emission spectrum at optical wavelengths only if it is produced by excitations of He II at temperatures around 1.4×10^5 K. Since the thermal velocity of helium at this temperature is about 25 km s^{-1}, which is comparable to the velocity difference between gas near the shock and gas in the recombination region, the radiative transfer is quite complicated and the following estimates are very rough.

The emitting region is about 10 scattering lengths thick at line center. To reach the region where photoionization of O II becomes important, the photons must pass through a region of higher density in which the absorption profile is somewhat narrower and somewhat shifted. Photons toward the red side of the original emission line will be unlikely to be scattered, while those toward the blue side must traverse about 40 mean free paths. If the emission region were not itself optically thick to this radiation, most of the photons on the short-wavelength side of the line would be scattered out through the shock front, but this region is thick enough that such photons are likely to be scattered back toward the cooler regions. The

scattering in the cooler gas will increase the distance traveled by the photons in traversing a given layer of gas, and hence increase the probability of absorption. The optical depth for photoionization processes in gas above 30,000 K is quite low, however; even with this increased path length taken into account, less than 0.1% of the 304 Å photons will be absorbed there. In the region where He I and He II coexist, the scattering could cause the absorption to occur in a narrower layer than assumed in the calculation, but because this happens at temperatures below 10,000 K, the absorption profile is quite narrow and relatively few photons will be affected. The many scatterings of the 304 Å line could give rise to Bowen fluorescence lines, but from the above estimates the number of scatterings should give Bowen lines less than 1% as strong as Hβ.

III. ATOMIC RATES

a) Atomic Data

Most of the formulae used for atomic rates in the model calculations are given by Raymond and Smith (1977). Gaunt factors not included in Table 3 of that paper are used for He I (Benson and Kulander 1972), and $2s$–$2p$ transitions of C III are from Flower and Launay (1973) and of N III, N IV, and O V are from Davis (1974). The Gaunt factors for excitation of hydrogenic, helium-like, lithium-like, and neon-like ions are taken from Mewe (1972), and those for beryllium-like ions are estimated from rates given by Johnston and Kunze (1971) and Tondello and McWhirter (1971). Excitation rates of Mg II are from Blaha (1972), those of Si II from Roberts (1970), and those of Ca II from Tully, Petrini, and Bely (1973). Line emission resulting from radiative recombination is included for hydrogen and helium, with rates from Brocklehurst (1971), Pengelly (1963), Robbins (1968), and Robbins and Robinson (1971).

Photoionization cross sections are those used by Raymond and Smith (1977). Photoionization of elements having $\chi < 13.6$ eV is estimated from the UV intensities given by Witt and Johnson (1973). The calculations include the charge exchange processes

$$O^+ + H \rightleftarrows O + H^+ , \qquad N^+ + H \rightleftarrows N + H^+ ,$$

with rates from Field and Steigman (1971) and Steigman (1975).

For forbidden and semiforbidden line radiation, the rate matrices are solved for the level populations using the methods of Cox (1970) except for the Fe III forbidden lines, which require the solution of a 17 × 17 matrix using collision strengths and transition probabilities calculated by Robb and Garstang (1975). The collision strengths, transition probabilities, and energy levels used for forbidden and semiforbidden lines are given in Raymond (1976). For a few transitions, excitation rates by neutral hydrogen and by protons are taken from Cox (1970). For fine-structure transitions in the boron-, fluorine-, aluminum-, and chlorine-isoelectronic sequences, proton excitation rates (Bely and Faucher 1970) and excitation by cascades from permitted line excitation are included. The cascade rates were estimated from permitted line excitation rates and branching ratios calculated from transition probabilities given by Wiese, Smith, and Glennon (1966) and Wiese, Smith, and Miles (1969).

b) Time-dependent Ionization Balance

The calculations begin with the ionization balance in the preshock gas and use the ionization and recombination rates to follow the population of each stage of ionization using the method described by Cox (1970). As the computer takes time steps following an element of gas, the ionization balance relaxes toward but does not reach the equilibrium ionization for the temperature of each step; the relaxation proceeds for the duration of the step.

The ionization balance of the preshock gas is generally taken to be the equilibrium ionization balance at the assumed preshock temperature, an equilibrium which may include the radiation flux calculated in an earlier model having the same v_s and scaled according to the preshock density. However, the recombination times of H, He II, and He III are on the order of $3 \times 10^5/n_e$, $10^5/n_e$, and $3 \times 10^4/n_e$ years, respectively, and the gas may not be in equilibrium. In some models the radiation flux from a faster shock is used, and occasionally some nonequilibrium state is specified. The ionization state of the preshock gas is thus taken to be essentially a free parameter.

IV. RESULTS

a) General Description

Tables 1 and 2 list the model parameters and flow characteristics for models of shocks in the range 50–200 km s^{-1}. The approximate treatment of the flow of neutrals into the shock is inadequate for calculation of shocks below 50 km s^{-1}, and shocks faster than 200 km s^{-1} associated with supernovae are unlikely to be in the radiative phase (Cox 1972*b*; Chevalier 1974) and cannot be described by the constant-flow models discussed here. The model parameters listed in Table 3 include preshock ionization fractions of H I, He I, and He II and the set of abundances (Table 2) used. The flow characteristics are postshock temperature and temperature at which hydrogen is half recombined [N(H I) = N(H II)], time and distance required for the gas to cool to 10^4 and 10^3 K, the minimum and secondary maximum temperatures of flows in which a temperature rise occurs in the recombination zone, and the total number of recombinations undergone by the average hydrogen and helium (He II → He I) atoms passing through the shock.

Tables 3 and 4 list the optical and ultraviolet spectra of the models and a few far-infrared lines which are important cooling mechanisms. Jenkins, Silk, and Wallerstein (1976) have derived column densities of many ions in filaments of the Vela supernova remnant. Table 5 lists the column densities predicted by the

TABLE 1

MODEL PARAMETERS AND FLOW CHARACTERISTICS

PARAMETER	MODEL A	B	C	D	E	F	G	H	I
v_s (km s^{-1})	50	60	70.7	81.5	100	120	141	160	200
n_0 (cm^{-3})	10	10	10	10	10	10	10	10	10
B_0 (μgauss)	1	1	1	1	1	1	1	1	1
Abundance set	A	A	A	A	A	A	A	A	A
R_{max}	1	1	1	1	1	1	1	1	1
f_0(H I)	0	0	0	0	0	0	0	0	0
f_0(He I)	0	0	0	1.	0.02	0	0	0	0
f_0(He II)	1.	1.	1.	0.	0.89	0.92	0.83	0.71	0.24
T_s (K)	39400	49800	69330	100300	152100	210500	285200	369100	569700
$T_{1/2}$ (K)	5360	5200	4890	4800	4800	4530	4680	6790	7340
t_{10000} (yr)	165	150	135	106	82	65	79	126	377
t_{1000} (yr)	720	540	430	850	1750	1710	1560	1530	1700
D_{10000} (cm $\times$ 10^{15})	4.0	3.9	3.5	2.8	2.1	1.7	2.7	6.5	35.
D_{1000} (cm $\times$ 10^{15})	6.1	5.2	4.3	4.3	5.6	5.0	5.7	9.1	3.7
T_{min} (K)	...	...	...	...	3360	4375	4643	5671	5795
T_{max} (K)	...	...	...	...	5760	6565	6703	7214	8253
H_{rec}	1.25	1.32	1.40	1.82	2.02	2.27	2.79	3.87	5.01
He_{rec}	1.17	1.20	1.27	1.72	2.76	3.54	4.13	4.06	5.18

PARAMETER	MODEL J	K	L*	M*	N	O	P	Q	R
v_s (km s^{-1})	60	70.0	50	60	100	100	100	100	100
n_0 (cm^{-3})	10	10	10	10	1	100	10	10	10
B_0 (μgauss)	1	1	1	1	0.01	1	0.1	10	1
Abundance set	A	A	A	A	A	A	A	A	A
R_{max}	1	1	1	1	1	1	1	1	1
f_0(H I)	0.1	0.1	0	0	0	0	0	0	0
f_0(He I)	0.31	0.31	0.1	0.1	0.98	0.17	0.02	0.98	0
f_0(He II)	0.69	0.69	0.9	0.9	0.02	0.82	0.91	0.02	0
T_s (K)	57800	77500	39800	56700	148000	151000	151000	148000	149000
$T_{1/2}$ (K)	5290	5650	5330	5000	5010	5850	5540	4890	4140
t_{10000} (yr)	61	77	183	160	767	8.2	81	96	109
t_{1000} (yr)	440	396	710	520	3431	316	1560	2500	546
D_{10000} (cm $\times$ 10^{15})	0.94	1.3	4.5	4.1	18.	0.20	2.1	3.0	3.7
D_{1000} (cm $\times$ 10^{15})	1.8	1.9	6.2	5.3	22.	0.57	3.6	31.	4.6
T_{min} (K)	...	...	...	...	...	5209	4250	3734	...
T_{max} (K)	...	...	...	...	...	6450	5370	6503	...
H_{rec}	1.17	1.27	1.24	1.33	1.75	1.92	1.88	1.73	1.92
He_{rec}	0.85	0.95	1.09	1.29	1.92	2.86	2.62	2.73	1.31

PARAMETER	MODEL S	T	U	V	W	X	Y	Z	AA
v_s (km s^{-1})	100	100	100	100	81.5	100	100	60	60
n_0 (cm^{-3})	10	10	10	10	10	10	10	300	350
B_0 (μgauss)	1	1	1	0.1	0.1	0.1	1	0.1	0.1
Abundance set	A	A	G1	G	G4	G3	G1	G2	A
R_{max}	0.3	3.	1	1	0.3	0.3	0.3	1.	0.3
f_0(H I)	0	0	0	0	0	0	0	0.1	0
f_0(He I)	0.02	0.98	0.02	0.98	0	0	0	0.35	0
f_0(He II)	0.91	0.02	0.91	0.02	0	0	0.91	0.65	1.
T_s (K)	151000	151000	151000	151000	97200	144000	156000	57800	58000
$T_{1/2}$ (K)	5110	5470	5900	7730	5770	5790	5850	6580	6010
t_{10000} (yr)	76	80	119	179	178	156	116	2.5	4.8
t_{1000} (yr)	92	1760	1550	18000	3850	4330	7000	150	72
D_{10000} (cm $\times$ 10^{15})	2.0	2.0	3.0	4.2	5.6	5.6	2.9	0.04	0.13
D_{1000} (cm $\times$ 10^{15})	3.5	5.5	5.9	20.	8.1	8.3	16.	0.20	0.20
T_{min} (K)	...	5430	5810	7600	...	4027	4419	...	...
T_{max} (K)	...	6240	7530	8510	...	4040	6160	...	...
H_{rec}	1.47	2.20	2.01	2.00	1.48	1.71	1.59	1.22	1.27
He_{rec}	1.72	3.33	3.29	3.64	1.24	1.37	2.18	0.85	1.21

TABLE 1—*Continued*

Parameter	Model BB	CC	DD	EE	FF	GG	HH	II	JJ
v_s (km s^{-1})	70.7	81.5	90	81.5	70.7	100	70.7	100	81.5
n_0 (cm^{-3})	10	1	12.5	15	300	10	300	200	200
B_0 (μgauss)	0.1	0.01	0.1	0.1	0.1	0.1	0.1	0.1	0.1
Abundance set	G	D	G5	G5	A	LMC	G	N	GG
R_{max}	1	1	3	3	1	1	1	1	1
f_0(H I)	0	0	0	0	0.2	0	0	0	0.2
f_0(He I)	0.31	1	0	0	0.3	0.18	1	0.98	0.34
f_0(He II)	0.69	0	0	0	0.7	0.81	0	0.02	0.66
T_s (K)	81200	95200	118000	97200	82700	153000	77500	151000	108000
$T_{1/2}$ (K)	7590	6150	5850	5770	6360	7170	7870	5340	6450
t_{10000} (yr)	341	1370	174	150	1.3	136	10.8	3.7	3.8
t_{1000} (yr)	905	10500	1660	1180	35	2970	2730	188	53
D_{10000} (cm $\times$ 10^{15})	9.3	35	6.0	4.8	0.017	3.0	0.30	0.09	0.05
D_{1000} (cm $\times$ 10^{15})	11.	46	7.4	5.8	0.055	6.7	2.7	0.26	0.10
T_{min} (K)	6480	...	...	...	...	6840	...	4730	...
T_{max} (K)	6540	...	...	...	...	8070	...	6160	...
H_{rec}	1.66	1.61	2.14	1.92	1.18	1.96	1.69	1.94	1.28
He_{rec}	1.95	1.66	1.59	1.43	0.89	3.24	1.86	2.89	0.98

* f_0(O II) = 0.31, f_0(O III) = 0.68.

TABLE 2

SETS OF ABUNDANCES

Element	A	G	G1	G2	G3	G4	G5	D	N	LMC
H	12.	12.	12.	12.	12.	12.	12.	12.	12.	12.
He	10.93	10.93	10.93	10.93	10.93	10.93	10.93	11.00	10.93	11.01
C	8.52	7.82	7.82	7.82	7.82	7.82	7.82	8.30	7.82	8.00
N	7.96	7.26	7.96	7.96	7.96	7.96	7.96	7.90	8.50	6.80
O	8.82	8.22	8.82	8.82	8.82	8.82	8.52	8.30	8.82	8.43
Ne	7.92	7.92	7.92	8.22	8.22	8.22	7.92	8.56	7.92	7.64
Mg	7.42	5.82	5.82	5.82	5.82	6.92	7.12	7.42	7.42	7.12
Si	7.52	5.82	5.82	5.82	5.82	5.82	7.22	7.20	7.52	7.50
S	7.20	6.90	6.90	7.20	7.50	7.50	7.20	7.00	7.20	5.01
Ca	6.30	2.80	2.80	6.30	6.00	6.00	6.00	...	6.30	5.80
Fe	7.60	6.90	6.90	6.90	6.90	6.90	7.30	...	7.60	7.20

TABLE 3

OPTICAL LINES 100 I_λ/Hβ: Hβ FLUX (ergs cm s^{-1} sr^{-1})

Line	Model A	B	C	D	E	F	G	H	I
Hβ	1.59–6	2.07–6	2.55–6	3.53–6	5.26–6	6.76–6	9.64–6	1.49–5	2.38–5
O II λ3726	610	652	537	349	260	273	287	284	273
O II λ3729	857	901	728	457	322	320	320	294	246
Ne III $\lambda\lambda$3868–3968	...	2.45	21.1	47.0	47.8	42.6	42.5	36.9	32.8
Ca II λ3945	31.6	18.7	14.1	9.76	14.9	16.9	19.1	18.4	27.5
S II $\lambda\lambda$4069–4076	13.9	13.5	12.6	10.0	9.57	12.2	12.6	11.8	14.7
Ca I λ4227	4.43	3.92	3.26	2.26	5.89	19.5	25.3	26.5	34.5
O III λ4363	...	3.13	16.9	26.0	25.4	26.0	30.7	27.9	20.0
Mg I λ4571	8.21	7.25	5.97	3.92	10.8	33.7	41.9	47.0	60.5
Fe III λ4658	36.8	39.4	40.7	34.8	35.6	49.9	56.8	60.0	69.5
He II λ4686	...	...	...	...	3.10	5.60	7.30	5.20	3.41
O III $\lambda\lambda$4959–5007	5.39	92.8	415	575	547	572	596	495	373
N I λ5198	3.66	3.13	2.42	1.54	5.50	13.4	15.6	12.3	13.5
N I λ5201	3.99	3.21	2.33	1.44	5.44	12.1	13.5	9.90	10.5
N II λ5755	7.73	8.18	6.96	5.08	3.90	3.95	3.87	3.21	2.67
He I λ5876	9.84	9.12	9.36	10.8	14.6	18.5	16.7	11.9	11.8
O I $\lambda\lambda$6300–6363	29.4	24.7	18.3	11.0	84.7	206	243	206	243
N II $\lambda\lambda$6548–6584	311	291	248	187	173	240	262	283	316
Hα	317	322	322	325	309	299	299	294	293
S II λ6717	90.6	84.6	76.5	58.9	65.3	91.6	93.6	82.5	92.3
S II λ6730	66.2	62.9	58.1	45.8	51.9	75.5	80.7	77.0	93.6
Ca II $\lambda\lambda$3291–7324	5.21	3.74	3.80	2.23	6.61	6.69	7.11	6.47	9.18
O II $\lambda\lambda$7320–7330	41.6	50.6	43.6	27.5	20.0	20.4	22.1	20.6	17.6
S III $\lambda\lambda$9069–9532	6.33	12.3	17.4	17.4	26.0	46.2	53.8	42.6	48.2
C I $\lambda\lambda$9823–9849	62.0	56.5	48.7	38.4	113	180	190	174	76.5
S II $\lambda\lambda$10284–336	7.58	7.36	6.83	5.40	5.13	6.60	6.84	6.43	8.01
He I λ10830	13.8	12.9	13.1	20.7	21.1	35.6	23.4	17.0	17.0

TABLE 3—*Continued*

Line	Model J	K	L	M	N	O	P	Q	R
Hβ	2.28–6	2.97–6	1.58–6	2.03–6	4.53–7	4.70–5	4.68–6	4.73–6	5.01–6
O II λ3726	282	414	348	435	290	287	304	203	323
O II λ3729	370	545	484	596	423	211	370	280	402
Ne III λλ3868–3968	...	1.65	9.07	14.1	56.2	55.8	54.5	45.8	57.7
Ca II λ3945	11.7	12.9	27.7	15.6	9.97	18.6	15.1	12.3	8.49
S II λλ4069–4076	6.58	9.72	12.5	13.0	9.10	21.4	11.2	7.33	9.02
Ca I λ4227	3.47	3.63	4.18	3.52	2.15	23.8	7.56	5.19	1.81
O III λ4363	...	2.78	17.9	22.0	29.6	28.9	28.7	25.9	35.7
Mg I λ4571	7.09	6.82	7.66	6.39	3.45	47.9	15.1	6.91	2.94
Fe III λ4658	22.1	28.4	36.9	40.0	32.6	62.0	*	30.0	35.9
He II λ4686	...	...	...	...	4.15	4.47	4.56	3.76	7.19
O III λλ4959–5007	46.3	95.7	581	556	637	649	622	587	625
N I λ5198	2.98	2.87	3.02	2.65	1.43	12.1	6.64	3.38	1.29
N I λ5201	2.95	2.70	3.25	2.69	1.80	8.42	5.90	4.10	1.14
N II λ5755	3.18	4.93	4.94	6.45	4.51	4.94	4.49	3.17	4.84
He I λ5876	5.93	6.14	9.22	9.42	12.8	16.5	16.0	16.6	7.97
O I λλ6300–6363	29.8	24.8	25.5	19.9	11.0	262	105	60.9	9.37
N II λλ6548–6584	186	217	238	254	169	259	207	150	169
Hα	*	*	325	323	330	299	304	302	318
S II λ6717	46.2	61.1	83.0	81.6	59.8	71.5	75.4	55.5	50.0
S II λ6730	36.0	47.1	60.7	60.8	42.6	95.2	61.8	40.3	40.6
Ca II λλ7291–7324	2.89	3.03	4.79	3.34	2.67	5.87	6.21	6.67	2.06
O II λλ7320–7330	15.4	28.1	21.3	31.1	21.3	36.2	23.0	15.7	26.6
S III λλ9069–9532	12.4	9.75	14.0	14.5	19.0	40.3	27.7	40.0	17.4
C I λλ9823–9849	64.1	67.2	58.6	51.9	23.8	267	178	30.0	33.1
S II λλ10284–330	2.78	4.10	6.78	7.05	4.94	11.6	6.04	3.97	4.90
He I λ10830	9.11	11.1	13.6	14.7	22.3	*	22.3	29.0	14.3

Line	Model S	T	U	V	W	X	Y	Z	AA
Hβ	3.85–6	5.34–6	5.03–6	4.96–6	3.11–6	4.37–6	3.91–6	7.00–5	6.76–5
O II λ3726	367	245	515	242	646	557	597	282	638
O II λ3729	454	299	645	301	851	700	752	178	478
Ne III λλ3868–3968	64.9	47.9	70.9	105	186	177	86.9	...	5.62
Ca II λ3945	11.9	14.2	...	...	8.07	7.84	...	18.5	20.4
S II λλ4069–4076	11.5	10.6	11.0	22.2	30.5	27.3	9.08	13.8	27.5
Ca I λ4227	2.92	13.6	...	...	2.48	2.49	...	7.60	6.23
O III λ4363	33.6	27.0	38.5	14.6	51.9	56.5	45.0	0.94	6.24
Mg I λ4571	5.18	23.5	2.02	4.79	2.83	...	...	...	12.0
Fe III λ4658	41.4	43.1	17.8	34.7	11.8	11.6	13.9	6.50	52.5
He II λ4686	3.98	3.47	5.22	4.32	11.6	10.5	5.92	...	...
O III λλ4959–5007	685	661	798	303	870	881	821	45.3	172
N I λ5198	2.04	8.33	34.5	18.2	3.89	4.10	16.2	2.01	1.38
N I λ5201	1.74	7.53	35.2	18.6	3.57	3.57	17.7	1.33	0.91
N II λ5755	5.60	3.42	7.16	2.71	9.39	8.08	8.69	4.16	9.65
He I λ5876	13.1	17.5	16.8	18.4	8.82	8.47	14.0	5.43	9.66
O I λλ6300–6363	16.4	134	467	269	36.1	50.2	235	64.4	42.2
N II λλ6548–6584	209	216	395	141	307	272	323	224	315
Hα	327	298	298	298	311	308	304	*	312
S II λ6717	64.0	80.9	89.2	175	176	155	64.9	27.5	48.7
S II λ6730	51.7	65.4	69.0	135	137	126	50.2	43.3	69.0
Ca II λλ7291–7324	2.56	5.95	...	...	2.12	2.80	...	4.28	4.12
O II λλ7320–7330	28.6	17.5	38.2	17.6	54.0	47.5	49.2	36.5	95.7
S III λλ9069–9532	18.0	49.5	33.7	56.2	56.7	51.9	19.5	10.1	15.2
C I λλ9823–9849	56.2	95.8	59.5	101	25.5	35.6	53.1	326	110
S II λλ10284–336	6.32	5.77	6.00	12.1	16.5	14.8	4.91	7.30	12.7
He I λ10830	17.6	29.2	24.8	32.8	12.4	11.9	20.3	152	257

TABLE 3—*Continued*

Line	Model BB	CC	DD	EE	FF	GG	HH	II	JJ
Hβ	2.96–6	3.31–7	6.00–6	5.96–6	7.88–5	4.63–6	8.95–5	9.61–5	7.00–5
O II λ3726	289	194	300	327	147	307	248	196	161
O II λ3729	392	285	375	411	88.4	375	181	125	105
Ne III λλ3868–3968	62.8	256	88.4	87.5	0.47	47.2	72.1	50.9	7.10
Ca II λ3945	...	...	9.59	9.25	9.57	30.4	...	13.1	17.0
S II λλ4069–4076	15.9	10.3	15.1	15.7	8.70	0.21	26.3	22.0	15.5
Ca I λ4227	...	...	4.82	3.86	4.01	23.9	...	19.3	6.14
O III λ4363	11.4	9.93	27.5	25.0	.87	19.4	10.7	26.5	1.81
Mg I λ4571	1.78	9.82	9.34	7.39	8.00	20.0	2.79	40.4	12.1
Fe III λ4658	23.0	...	9.89	30.6	*	*	27.2	53.3	37.1
He II λ4686	0.45	0.54	6.75	4.94	...	5.28	0.43	3.74	...
O III λλ4959–5007	223	207	433	409	44.5	422	210	598	64.1
N I λ5198	6.88	3.94	5.69	4.50	0.92	3.73	4.80	26.4	14.1
N I λ5201	7.63	5.21	4.81	3.83	0.60	3.56	3.39	17.6	9.29
N II λ5755	3.09	8.00	8.32	9.17	2.49	0.70	3.31	15.2	4.76
He I λ5876	11.3	13.4	8.10	7.98	5.40	21.7	11.0	16.6	5.30
O I λλ6300–6363	112	14.0	38.5	26.8	43.5	278	132	233	23.1
N II λλ6548–6584	117	287	316	322	139	38.7	118	718	207
Hα	301	312	302	307	*	308	300	299	*
S II λ6717	123	70.0	91.5	90.8	13.9	1.55	70.0	47.2	29.8
S II λ6730	91.2	49.4	76.5	75.4	23.9	1.23	95.6	76.2	45.9
Ca II λλ7291–7324	...	...	2.79	2.41	2.33	8.52	...	4.42	3.66
O II λλ7320–7330	23.3	15.0	25.3	27.8	21.9	21.8	39.0	36.2	23.5
S III λλ9069–9532	26.7	16.5	37.0	34.1	11.4	0.55	25.4	35.1	8.11
C I λλ9823–9849	60.5	25.5	19.9	18.0	72.3	134	98.4	220	21.8
S II λλ10284–336	8.63	5.55	8.17	8.55	4.71	...	14.2	12.0	8.40
He I λ10830	21.1	30.0	19.2	11.3	164	38.0	*	*	185

* Line was not calculated.

TABLE 4

UV AND IR LINES ($100I_\lambda/H\beta$)

Line	Model A	B	C	D	E	F	G	H	I
Lα	4850	4720	4530	4200	4210	4500	5080	5120	4450
C II 1336 Å	333	497	508	366	289	267	169	87	73
C II] 2324 Å	481	550	522	400	324	304	200	116	112
C III 977 Å	14	196	725	1140	1240	1190	1010	329	296
C III] 1910 Å	35	235	568	707	657	638	513	202	195
C IV 1549 Å	...	...	18	146	756	1610	2580	1080	612
N III 991 Å	...	10	47	78	84	90	127	108	53
N V 1240 Å	...	...	...	...	1	10	120	496	407
[O II] 2471 Å	115	140	120	76	55	56	61	57	49
O III] 1664 Å	...	17	102	171	176	180	229	221	157
O IV] 1401 Å	...	...	...	3	27	58	130	197	159
O V 1213 Å	...	...	...	...	...	3	39	202	402
O VI 1034 Å	...	...	...	...	...	...	6	253	494
Mg II 2798 Å	202	114	64	36	34	37	34	26	31
Si II 1263 Å	156	162	142	107	79	52	32	29	24
Si III 1206 Å	147	465	780	765	550	326	139	137	141
Si IV 1397 Å	...	2	21	62	107	100	51	37	53
S III 1198 Å	15	86	189	202	171	177	214	180	125
[C II] 156 μm	25	18	12	25	43	40	30	21	19
[O I] 63 μm	28	24	21	36	103	128	125	98	97
[Ne II] 12.8 μm	42	39	36	42	79	98	99	84	84
[Si II] 34.8 μm	285	254	212	370	593	618	539	412	364
[Fe II] 26 μm	56	50	46	81	131	140	136	110	109

TABLE 4—*Continued*

Line	Model J	K	L	M	N	O	P	Q	R
Lα.....	7440	7090	4310	4320	4030	4290	4220	4310	3970
C II 1336 Å.....	83	195	250	424	328	341	326	241	340
C II] 2324 Å.....	155	290	391	503	373	392	366	272	363
C III 977 Å.....	26	92	145	422	1330	1370	1380	1230	2260
C III] 1910 Å.....	56	136	237	409	759	740	736	685	1050
C IV 1549 Å.....	...	...	3	5	815	796	842	710	1720
N II 916 Å.....	10	25	17	46	45	45	42	34	55
N III 991 Å.....	1	5	16	37	98	97	95	86	158
N IV 1490 Å.....	...	...	1	1	14	14	17	12	27
N V 1240 Å.....	...	...	...	...	1	1	1	...	3
[O II] 2471 Å.....	42	76	59	85	59	102	64	43	73
O III] 1664 Å.....	4	13	87	128	202	202	198	179	269
O IV] 1401 Å.....	...	...	...	...	24	26	30	19	49
O V 1213 Å.....	...	...	...	...	...	...	...	...	1
O VI 1034 Å.....	...	...	...	...	...	...	...	...	...
Mg II 2798 Å.....	70	48	162	83	33	47	38	22	27
Si II 1263 Å.....	39	89	117	140	89	97	90	58	72
Si III 1206 Å.....	55	155	198	525	636	634	617	552	638
Si IV 1397 Å.....	...	1	14	16	124	119	119	115	204
S III 1198 Å.....	12	33	48	123	194	194	192	168	260
[C II] 156 μm.....	11	10	25	17	86	9	41	66	13
[O I] 63 μm.....	30	31	27	20	46	151	148	46	35
[Ne II] 12.8 μm.....	34	35	41	37	44	110	92	57	35
[Si II] 34.8 μm.....	240	228	280	230	607	310	712	450	250
[Fe II] 26 μm.....	55	55	55	48	114	173	167	73	72

Line	Model S	T	U	V	W	X	Y	Z	AA
Lα.....	4330	4280	4600	4690	4730	4350	4360	7600	4730
C II 1336 Å.....	334	273	106	175	145	119	127	19	584
C II] 2324 Å.....	440	312	115	202	143	119	269	38	634
C III 977 Å.....	1670	1180	381	557	595	771	477	6	345
C III] 1910 Å.....	884	656	209	328	325	350	264	12	363
C IV 1549 Å.....	1020	693	198	238	82	577	248	...	2
N II 916 Å.....	52	35	75	27	116	101	93	11	95
N III 991 Å.....	113	85	132	41	199	268	161	...	19
N IV] 1490 Å.....	20	12	18	4	9	47	24	...	...
N V 1240 Å.....	1	1	1	...	...	6	...	...	...
[O II] 2471 Å.....	79	48	105	49	149	132	137	101	264
O III] 1664 Å.....	235	180	272	102	385	448	182	4	34
O IV] 1401 Å.....	36	21	33	9	11	82	83	...	...
O V 1213 Å.....	...	...	...	...	...	1	...	...	...
O VI 1034 Å.....	...	...	...	...	...	...	...	...	...
Mg II 2798 Å.....	38	37	2	6	17	1	2	2	99
Si II 1263 Å.....	108	75	3	4	4	2	3	1	166
Si III 1206 Å.....	747	537	19	30	35	19	23	1	650
Si IV 1397 Å.....	144	107	3	4	3	6	4	...	5
S III 1198 Å.....	232	166	150	240	959	917	222	14	134
[C II] 156 μm.....	34	48	58	114	31	29	64	1	1
[O I] 63 μm.....	49	105	254	147	174	227	256	78	58
[Ne II] 12.8 μm.....	48	89	115	137	98	109	46	84	53
[Si II] 34.8 μm	433	636	25	34	17	19	42	4	92
[Fe II] 26 μm.....	98	135	41	51	35	40	44	23	75

TABLE 4—*Continued*

Line	Model BB	CC	DD	EE	FF	GG	HH	II	JJ
Lα.....	4720	4600	4830	4690	8220	4510	4510	4410	8330
C II1336 Å.....	224	402	128	142	63	202	225	281	31
C II] 2324 Å....	228	423	124	137	108	235	231	333	51
C III 977 Å.....	431	853	747	604	34	665	394	1200	24
C III] 1910 Å....	303	565	360	326	59	385	286	659	33
C IV 1549 Å....	19	58	266	87	...	320	16	719	...
N II 916 Å.....	37	90	108	117	9	7	37	130	20
N III 991 Å.....	28	84	250	202	1	11	26	294	6
N IV] 1490 Å...	...	1	22	9	...	...	...	43	...
N V 1240 Å.....	...	...	1	...	...	...	...	...	...
[O II] 2471 Å....	64	41	70	77	60	60	108	100	65
O III] 1664 Å....	77	66	214	188	4	134	71	178	8
O IV] 1401 Å....	...	...	17	6	...	13	...	22	...
O V 1213 Å.....	...	...	...	...	...	...	...	...	...
O VI 1034 Å....	...	...	...	...	...	...	...	...	...
Mg II 2798 Å....	4	79	26	28	36	21	3	36	53
Si II 1263 Å.....	6	90	76	93	23	157	6	77	66
Si III 1206 Å....	40	546	741	872	62	1100	38	548	156
Si IV 1397 Å....	2	29	141	89	...	158	1	109	3
S III 1198 Å.....	256	189	487	484	15	2	243	166	37
[C II]156μm....	179	183	9	7	...	25	23	5	...
[O I] 63 μm.....	117	27	57	47	30	102	175	135	19
[Ne II]12.8μm...	70	25	57	51	35	67	86	108	74
[SiII] 34.8μm....	33	466	332	302	41	964	21	201	59
[Fe II] 26 μm....	50	...	76	72	60	69	53	179	69

models for ions which have observable UV absorption lines, but it should be kept in mind that a shock may be followed by an extensive cloud of cold gas having substantial amounts of C II, N I, O I, Si II, S II, and Fe II. Populations of the excited fine-structure levels of C II, O I, Ne II, Si II, and Fe II can be calculated from the intensities of the forbidden lines listed in Table 3. The fine-structure levels of C I are populated nearly according to their statistical weights in all models.

The present section will give a detailed description of model E, a 100 km s^{-1} shock moving into an ionized gas having a preshock density of 10 cm^{-3}. This model assumes cosmic abundances (Allen 1973), a transverse magnetic field of 1 μgauss, and $R_{max} = 1$. Variations in each of these parameters will be considered in § IV*b*.

The gas flowing into the shock front in model E is for the most part singly ionized. At the shock it is heated to about 1.5×10^5 K and compressed by almost a factor of 4. The equilibrium ionization balance of helium at this temperature is 0.99 He^{+2}, 0.01 He^{+}, so the singly ionized helium entering the shock begins to be further ionized. The ratio of the

TABLE 5

COLUMN DENSITIES (10^{14} cm^{-2})

Ion	Model A	B	C	D	E	F	G	H	I
C I.....	0.91	0.83	0.76	2.2	3.8	3.8	4.0	4.4	1.6
C II.....	2.9	2.5	2.2	6.0	15.	18.	19.	20.	29.
C III.....	0.046	0.17	0.32	0.45	0.76	0.91	1.0	0.80	1.0
N I	0.51	0.42	0.38	1.7	4.2	4.7	4.9	5.2	6.7
N II.....	0.55	0.51	0.43	0.51	0.98	1.2	1.4	1.6	1.9
N III.....	0.005	0.039	0.10	0.14	0.23	0.31	0.39	0.34	0.31
N V.....	...	...	...	...	...	0.001	0.018	0.12	0.18
O I.....	3.4	2.8	2.5	13.	32.	37.	39.	41.	53.
O VI.....	...	...	...	...	...	...	0.001	0.086	3.1
Si II.....	0.27	0.24	0.21	0.62	1.6	1.9	2.1	2.3	3.0
Si III.....	0.033	0.051	0.061	0.064	0.078	0.088	0.099	0.12	0.15
Si IV.....	...	...	0.002	0.006	0.013	0.014	0.012	0.010	0.017
S I.....	0.048	0.39	0.030	0.056	0.13	0.13	0.13	0.14	0.053
S II.....	0.13	0.12	0.11	0.32	0.73	0.83	0.87	0.96	1.3
S III.....	0.005	0.013	0.019	0.031	0.083	0.12	0.14	0.13	0.16
S IV.....	...	...	0.001	0.004	0.008	0.010	0.016	0.18	0.016
Ca II.....	0.006	0.005	0.003	0.022	0.044	0.037	0.034	0.042	0.046
Fe II.....	0.29	0.23	0.20	0.73	2.0	2.3	2.4	2.6	3.4
Fe III.....	0.096	0.10	0.093	0.085	0.10	0.12	0.14	0.17	0.20

TABLE 5—*Continued*

Ion	Model J	K	L	M	N	O	P	Q	R
C I	1.0	1.1	0.89	0.80	0.75	6.9	3.8	1.9	1.3
C II	1.7	1.9	2.8	2.4	2.9	27.	13.	23.	4.0
C III	0.096	0.12	0.22	0.27	0.39	0.75	0.60	2.4	0.60
N I	0.45	0.48	0.50	0.41	0.69	8.5	3.8	3.7	1.0
N II	0.32	0.35	0.46	0.44	0.28	0.96	0.66	2.8	0.46
N III	0.012	0.027	0.11	0.10	0.13	0.22	0.17	1.1	0.17
N V	...	...	...	...	...	...	...	...	...
O I	3.0	3.3	3.3	2.7	5.1	64.	29.	33.	7.3
O VI	...	...	...	...	...	...	...	...	...
Si II	0.21	0.23	0.26	0.22	0.25	3.2	1.4	2.4	0.40
Si III	0.018	0.024	0.038	0.055	0.044	0.082	0.064	0.26	0.52
Si IV	...	...	0.002	0.002	0.011	0.012	0.012	0.026	0.022
S I	0.053	0.055	0.046	0.036	0.027	0.20	0.13	0.063	0.039
S II	0.076	0.089	0.13	0.11	0.14	1.4	0.62	0.94	0.21
S III	0.006	0.006	0.011	0.016	0.20	0.093	0.058	0.30	0.026
S IV	...	...	0.001	0.001	0.007	0.007	0.007	0.017	0.014
Ca II	0.004	0.004	0.006	0.004	0.012	0.049	0.033	0.058	0.011
Fe II	0.21	0.22	0.27	0.21	0.32	3.6	1.7	2.8	0.47
Fe III	0.058	0.064	0.098	0.10	0.060	0.10	0.083	0.35	0.076

Ion	Model S	T	U	V	W	X	Y	Z	AA
C I	4.3	1.8	1.7	2.2	1.4	1.8	2.2	3.5	12.
C II	8.7	17.	20.	37.	6.3	8.2	17.	2.9	6.2
C III	0.45	0.93	0.25	0.30	0.15	0.17	0.18	0.020	0.22
N I	3.1	4.0	28.	11.	10.	13.	26.	8.2	4.4
N II	0.50	1.0	1.6	0.37	0.51	0.55	1.1	0.51	0.56
N III	0.13	0.32	0.38	0.10	0.21	0.24	0.21	0.013	0.057
N V	...	...	...	...	...	...	...	...	...
O I	22.	31.	210.	95.	73.	97.	190.	59.	31.
O VI	...	...	...	...	...	...	...	...	...
Si II	0.95	1.8	0.21	0.38	0.062	0.085	0.17	0.059	1.3
Si III	0.049	0.096	0.003	0.003	0.002	0.001	0.002	...	0.060
Si IV	0.012	0.014	...	...	...	...	...	...	...
S I	0.13	0.052	0.17	0.22	0.55	0.74	0.30	0.58	0.38
S II	0.48	0.76	2.4	4.4	3.1	4.1	2.0	0.93	0.47
S III	0.032	0.11	0.079	0.087	0.078	0.082	0.049	0.007	0.016
S IV	0.007	0.008	0.006	0.007	0.19	0.043	0.003	...	...
Ca II	0.040	0.044	...	...	0.087	0.11	0.001	0.068	0.012
Fe II	1.2	2.1	2.4	4.4	0.81	1.1	2.1	0.67	1.2
Fe III	0.070	0.12	0.030	0.035	0.021	0.018	0.023	0.014	0.11

Ion	Model BB	CC	DD	EE	FF	GG	HH	II	JJ
C I	1.7	0.47	0.47	0.50	4.9	1.7	7.1	7.9	1.1
C II	35.	5.0	3.6	2.8	1.9	7.4	130.	33.	0.57
C III	0.22	0.31	0.24	0.20	0.099	0.32	0.20	0.69	0.028
N I	9.9	1.7	4.9	3.9	1.6	0.49	38.	36.	2.0
N II	0.30	0.49	0.75	0.69	0.29	0.087	0.34	3.1	0.39
N III	0.059	0.13	0.32	0.27	0.014	0.024	0.055	0.68	0.035
Nv	...	...	...	...	...	...	...	...	...
O I	90.	4.2	18.	14.	12.	22.	350.	77.	7.0
O VI	...	...	...	...	...	...	...	...	...
Si II	0.36	0.35	0.96	0.77	0.57	2.6	1.4	3.8	0.74
Si III	0.004	0.040	0.60	0.066	0.018	0.12	0.004	0.076	0.023
Si IV	...	0.003	0.016	0.009	...	0.015	...	0.011	...
S I	0.20	0.028	0.059	0.060	0.20	0.001	0.44	0.22	0.23
S II	4.2	0.24	0.89	0.71	0.13	0.007	16.0	1.7	0.18
S III	0.047	0.021	0.063	0.055	0.007	...	0.004	0.084	0.007
S IV	0.003	0.002	0.021	0.012	...	...	...	0.007	...
Ca III	...	...	0.033	0.025	0.005	0.020	...	0.053	0.008
Fe II	4.3	...	1.1	0.87	0.58	1.2	16.	4.3	0.77
Fe III	0.042	...	0.069	0.70	0.048	0.055	0.041	0.092	0.057

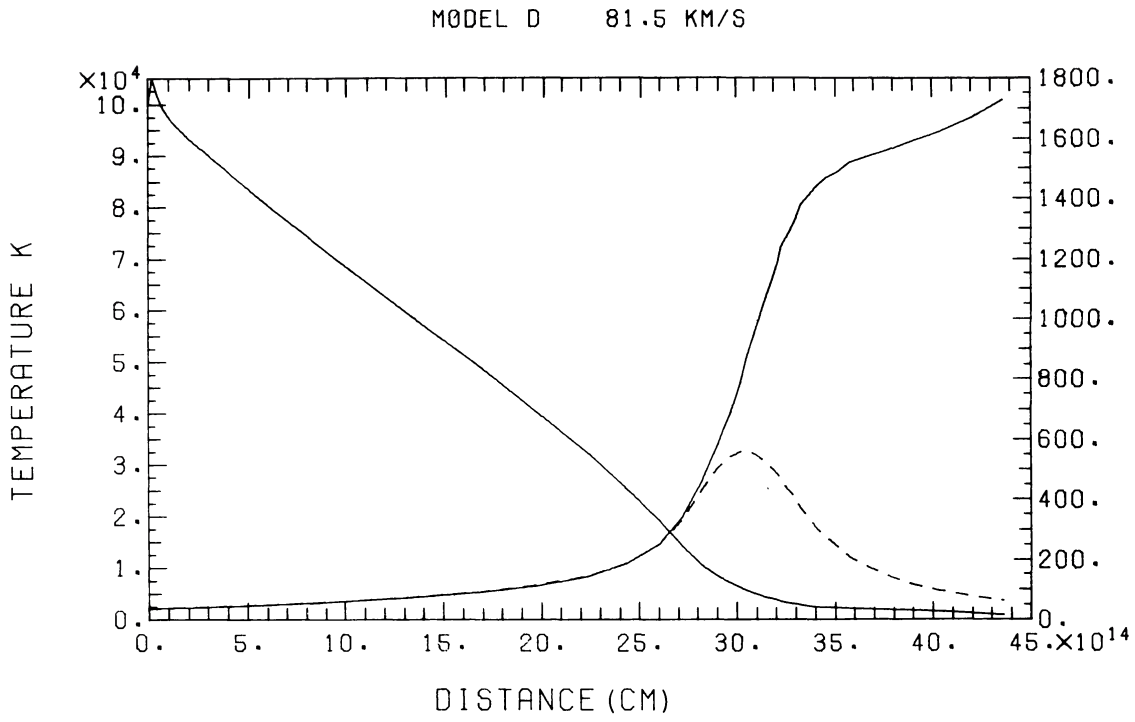

FIG. 1*a*

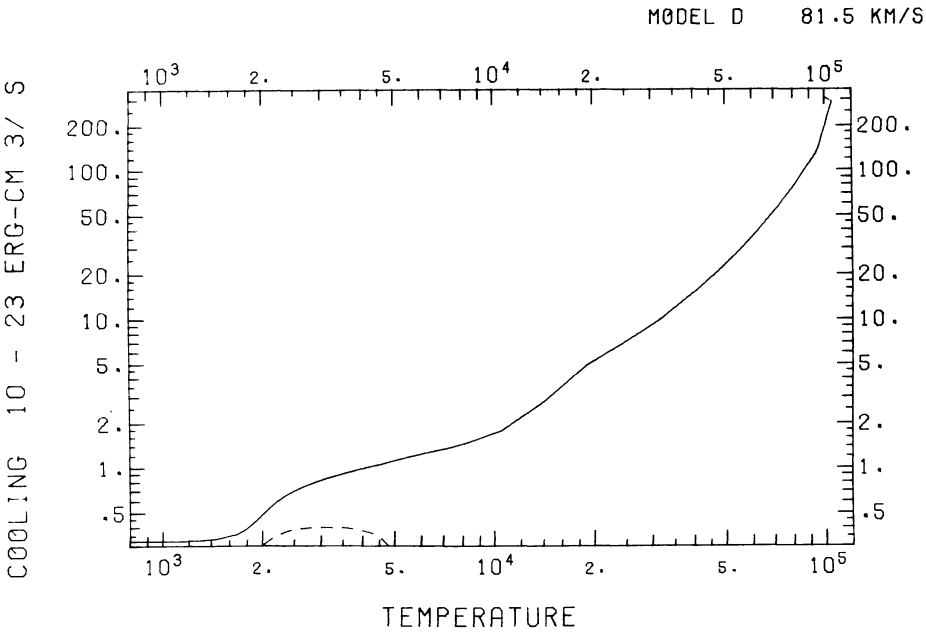

FIG. 1*b*

FIG. 1.—(*a*) Temperature, density, and (*dashed curve*) electron density, and (*b*) cooling and (*dashed curve*) heating rates for model D. Ionization fractions of (*c*) helium and (*d*) oxygen for model D.

rate of 1*s*–2*p* excitation to the rate of collisional ionization of He II is $\sim 2.5 \exp(13.6\ \mathrm{eV}/kT)$, the exponential being due to the difference between the 1*s*–2*p* excitation energy and the ionization potential. At 1.5×10^5 K this ratio is about 7, and roughly 290 eV is radiated in the He II 304 Å line for each ionization of He II. At the lower temperatures found farther back in the flow this ratio increases, and of a total postshock enthalpy of 85 eV per nucleus in this model, 19 eV is lost in the 304 Å line. Helium reaches a maximum ionization state of 0.29 He III, 0.71 He II about 17 years after passing through the shock front. The gas temperature there is about 77,000 K. Similarly, carbon is mostly helium-like C V in equilibrium

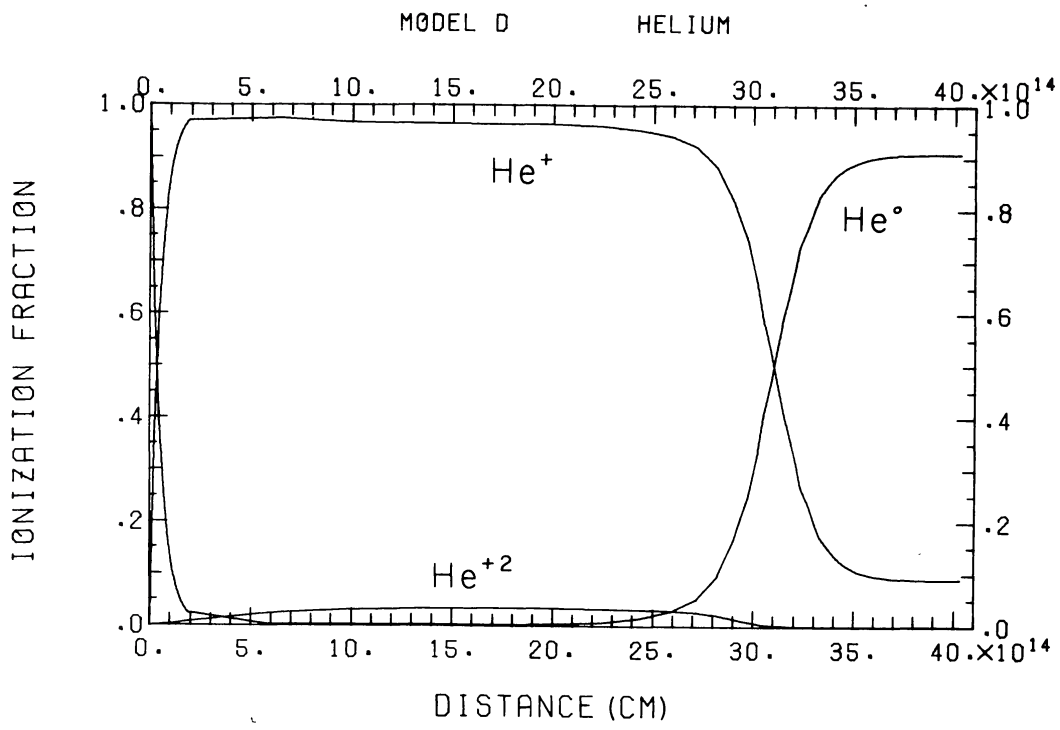

FIG. 1c

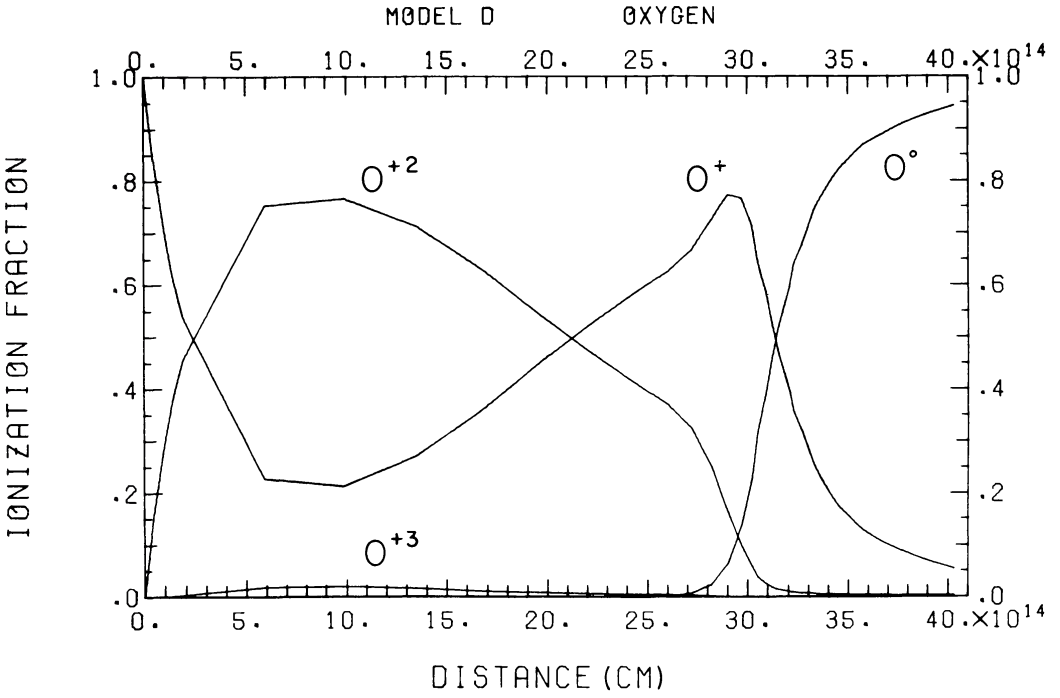

FIG. 1d

FIG. 1.—*Continued*

at 1.5×10^5 K, but carbon flowing through the shock reaches a maximum ionization of 0.65 C III, 0.31 C IV. The ionization state, temperature, density, and cooling rate of model E are shown in Figure 2, and similar plots for faster and slower shocks are shown in Figures 1 and 3.

The presence of C III, C IV, and He II in the high-temperature gas behind the shock increases the radiative cooling rate by a factor of 5–10 over the equilibrium cooling rate. This accounts for most of the differences between models C and G and models at the same velocities calculated by Cox (1972*a*), who

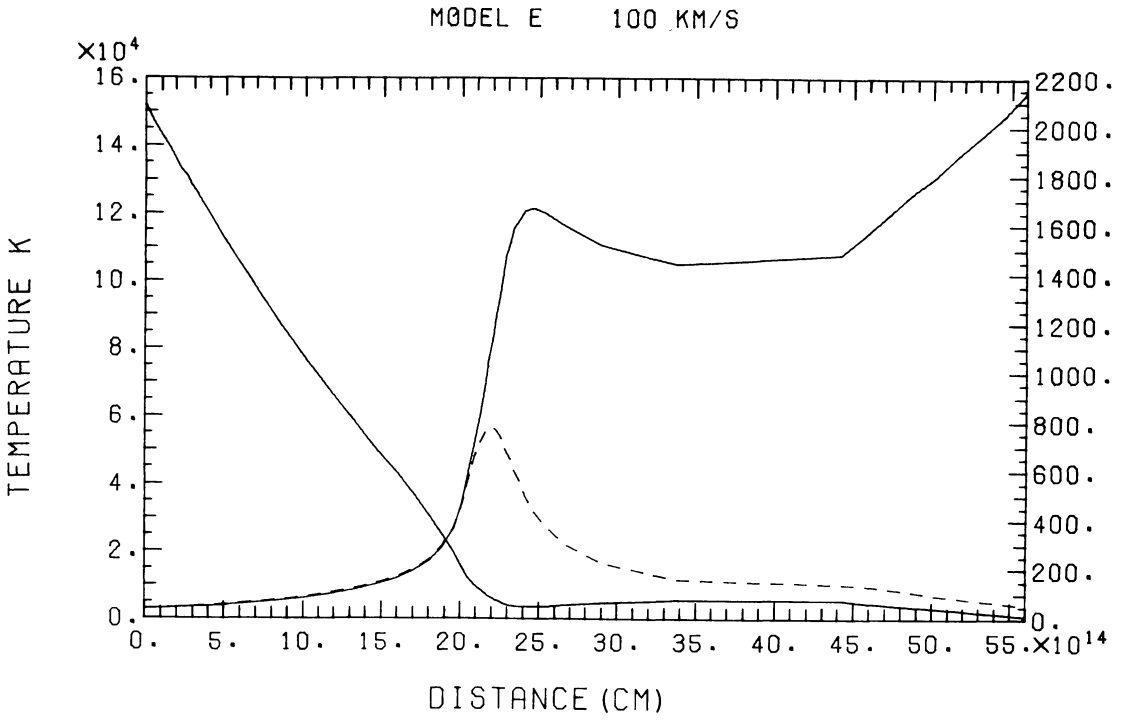

FIG. 2a

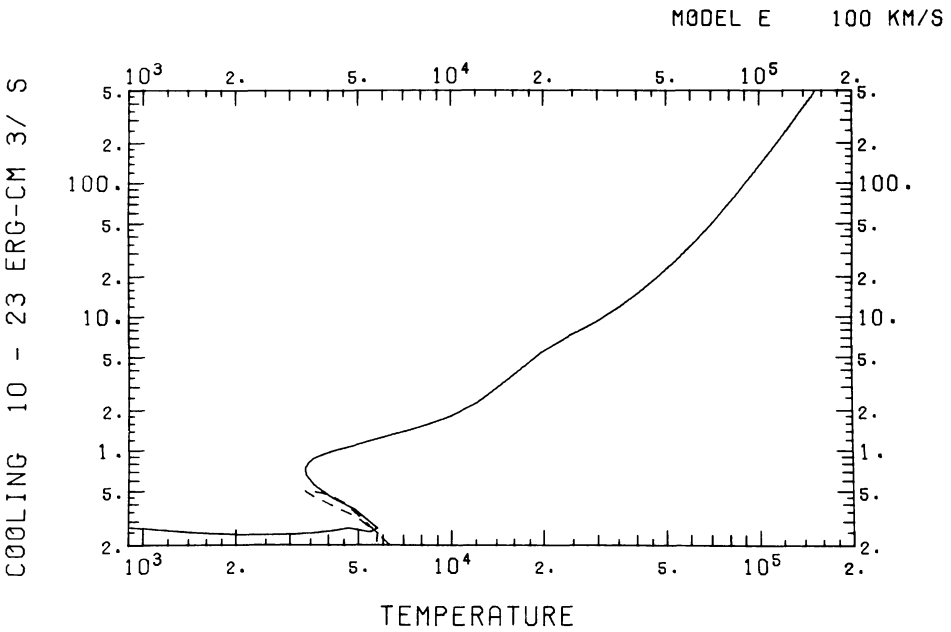

FIG. 2b

FIG. 2.—Same as Fig. 1 for model E

assumed ionization equilibrium at the postshock temperature as the starting point for calculating the nonequilibrium ionization balance in the rest of the flow. The high cooling rates in the present models cause a much steeper temperature drop than in Cox's models. A side effect of this cooling is the increased photoionization rates of He I and singly ionized species of other elements by the He II 304 Å photons. In the case of He I, these photoionizations simply result in additional recombinations, roughly doubling the strengths of the He I recombination lines. Because the He I photoionization cross section at 304 Å is 11 times larger than that of hydrogen, helium is more strongly affected. In passing through the shock and recombination region, an average helium atom recombines 2.76 times, compared to 2.03 times for a

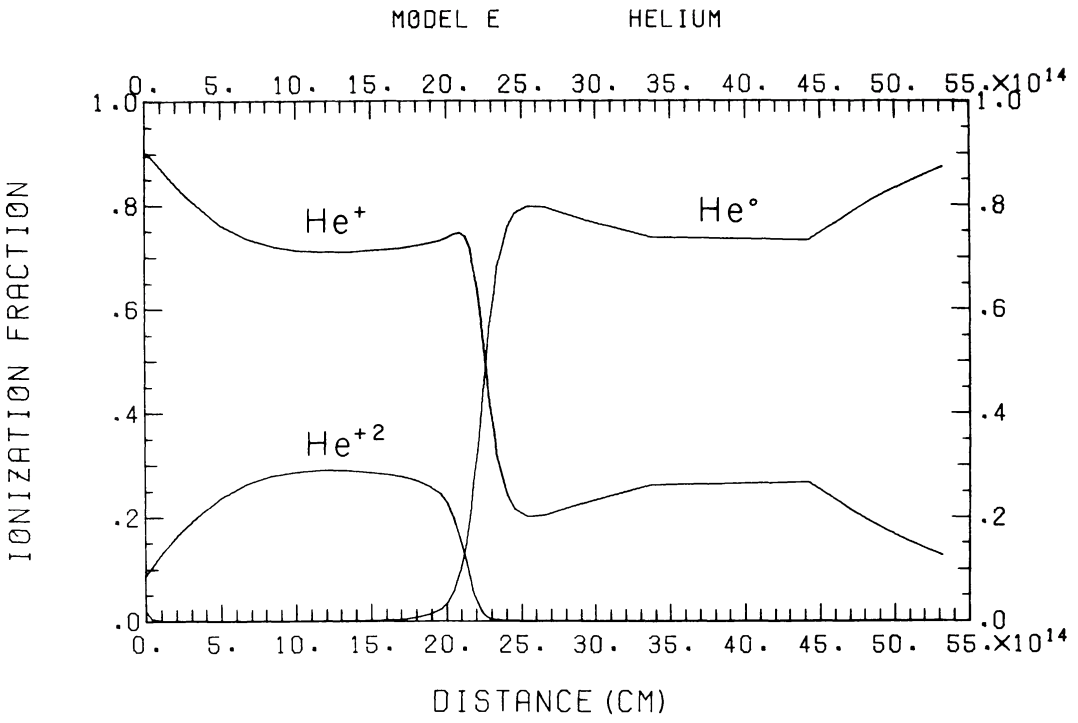

FIG. 2c

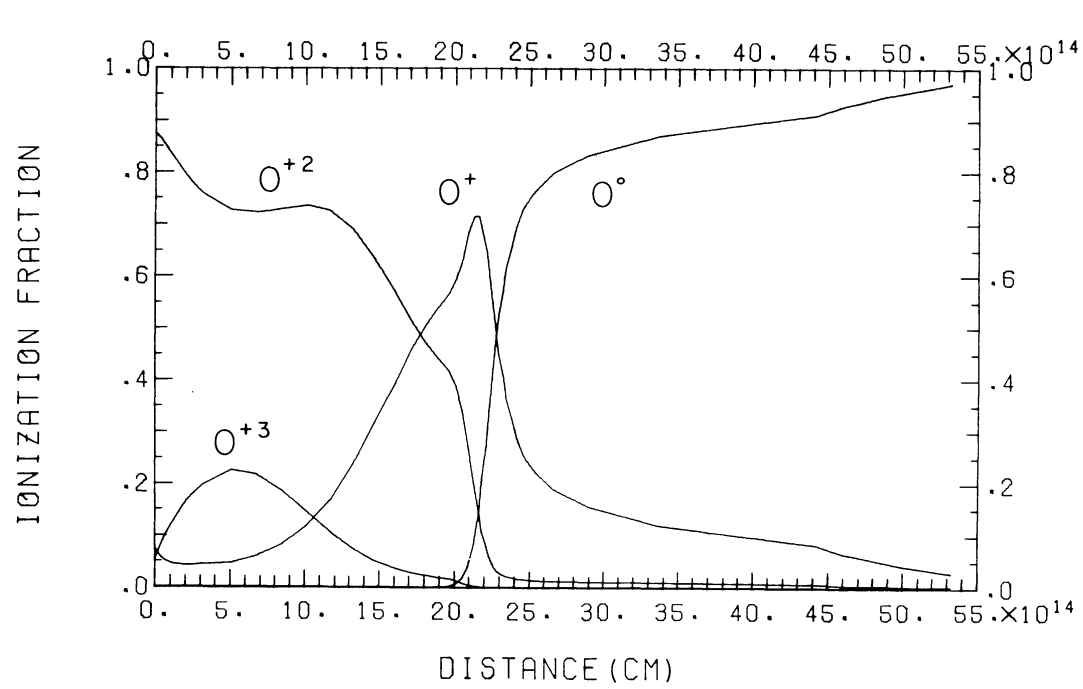

FIG. 2d

FIG. 2.—*Continued*

hydrogen atom. Photoionization of O II by the 304 Å photons lowers the temperature at which half of the O III has recombined to O II from about 50,000 to about 30,000 K. This causes a significant increase in the intensity of the [O III] lines and a lowering of the temperature which they indicate and a weakening of the [O II] lines.

When the gas cools to about 30,000 K, Lα and forbidden and semiforbidden lines become the dominant cooling mechanisms because of the high energies

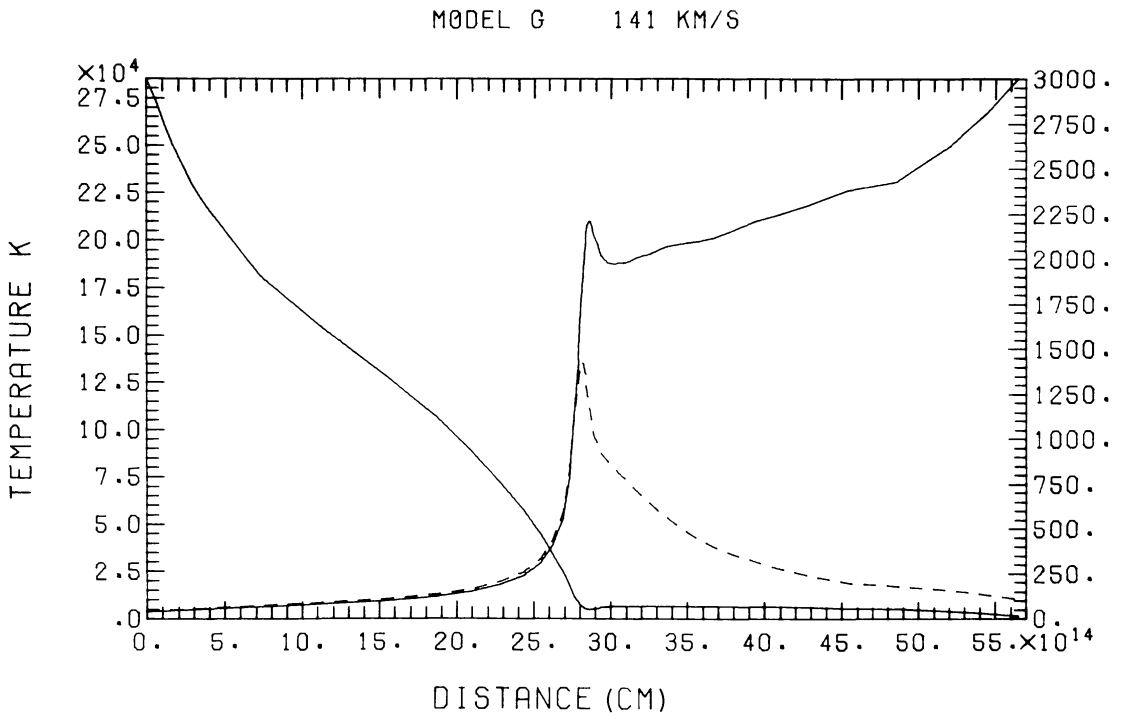

FIG. 3a

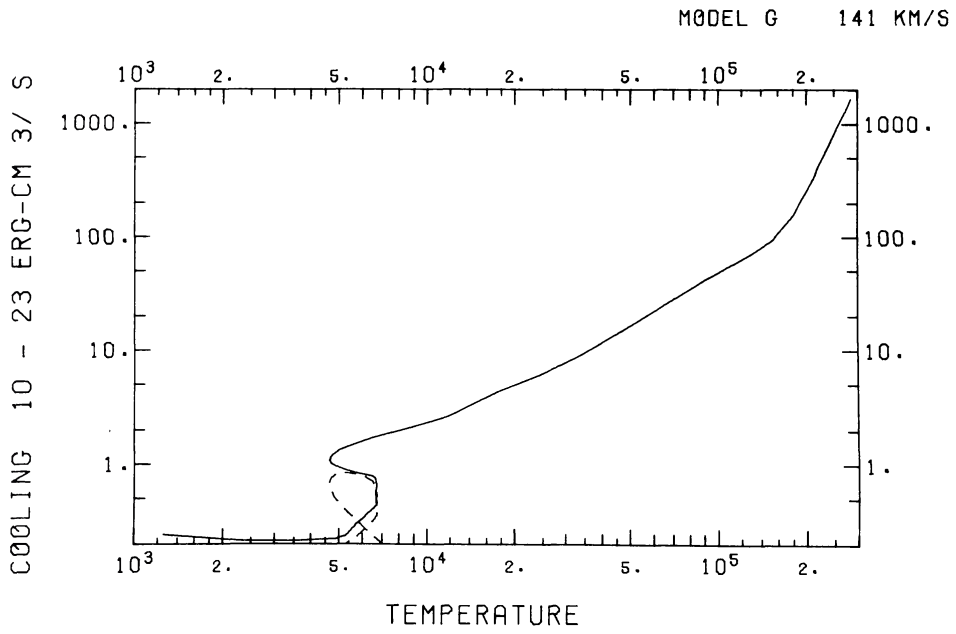

FIG. 3b

FIG. 3.—Same as Fig. 1 for model G

needed to excite most permitted lines. At still lower temperatures, recombination and excitation of infrared forbidden lines become the most important mechanisms for emission of radiation.

When the gas reaches 12,000 K, hydrogen is one-tenth neutral; at 4500 K it is half neutral. The sudden availability of neutral hydrogen to absorb EUV photons produced upstream causes a sharp increase in the rate of heating by photoionization. In this particular model, the heating rate never becomes as large as the cooling rate; but since most of the cooling is due to recombinations and since recombinations preferentially remove slow free electrons from the gas as well as energy, the average thermal energy per particle begins to rise. In this case the temperature reaches a minimum of 3360 K, then rises to 5760 K as

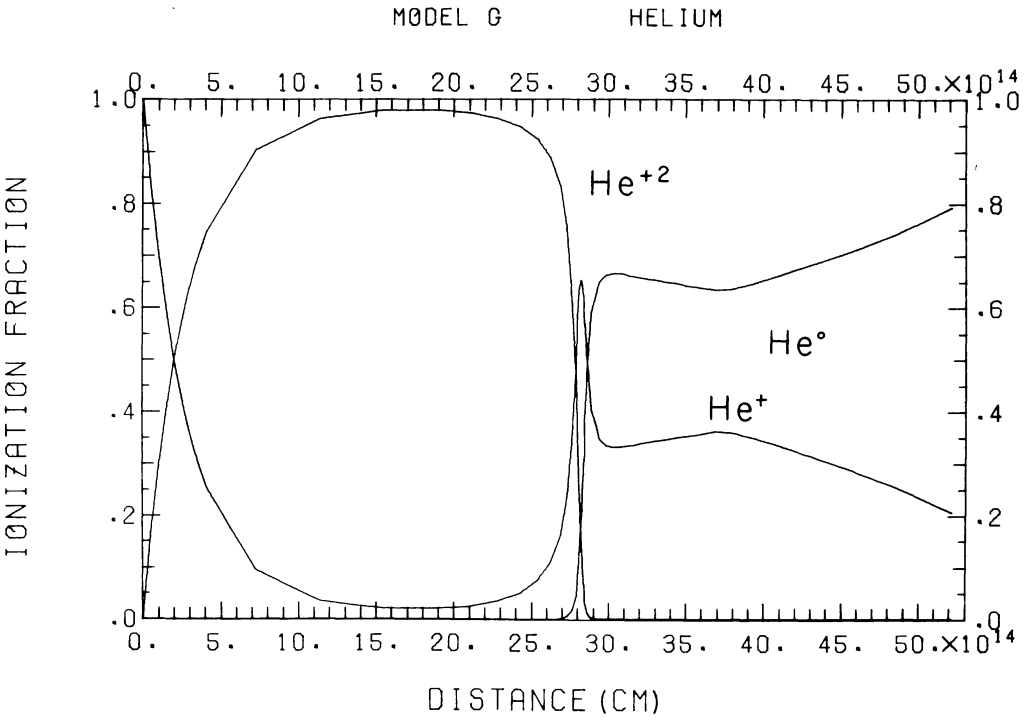

FIG. 3c

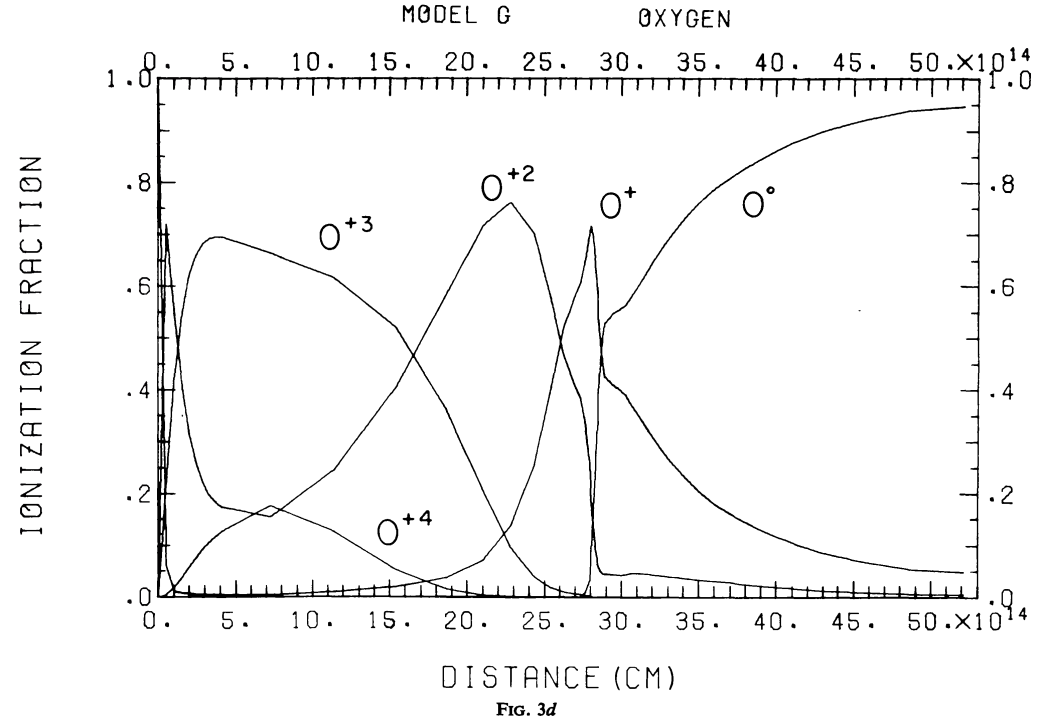

FIG. 3d

FIG. 3.—*Continued*

hydrogen recombines to become 92% neutral. By the time the gas reaches the secondary temperature peak at 5760 K, it is effectively shielded from hydrogen-ionizing radiation produced upstream (τ_{912} Å = 7). The temperature then falls slowly as the gas cools by emission of far-infrared lines of C II, O I, Si II, and Fe II. As recombination removes the free electrons, the recombination rate becomes smaller than the photoionization rate for elements which can be ionized by the unabsorbed photons longer than 912 Å. Magnesium, for example, is 71% neutral at 3400 K and is reionized to 38% Mg I, 62% Mg II at 1000 K.

Model E assumes a transverse magnetic field of 1 μgauss in the preshock gas. Compression of this field by a factor of 230 would result in a magnetic pressure equal to the total ram pressure driving the shock, so this value is an upper limit to the compression of the gas. At the temperature minimum at 3360 K, the compression factor is found to be 169 and just over half of the total pressure is due to the magnetic field. The temperature rise increases the thermal pressure and reduces the compression to 145. The calculation is terminated when the gas reaches 500 K, and the compression factor there is 220.

The Hβ emission from this model shock is 5.34×10^{-6} ergs cm^{-2} s^{-1} sr^{-1}, 97% of which results from recombinations and the rest from collisional excitations. The Hα line is 3.09 times as intense, 95.6% being due to recombinations. The other prominent optical lines are the forbidden lines of oxygen, nitrogen, sulfur, and neon. The [O III] $I(4959+5007)/I(4363)$ ratio (where the wavelengths are in angstroms) is characteristic of emission at a single temperature with $T = 31{,}000$ K, the [O II] $I(7320\text{–}7330)/I(3727)$ ratio corresponds to emission at 20,000 K at low density, and the [N II] $I(6548+6584)/I(5755)$ ratio corresponds to 15,000 K. The near-infrared emission is dominated by He I 10830 and [C I] 9823–9850 Å. In the ultraviolet, Lα is more than 3 times as strong as any other line, but the resonance lines of C II, C III, and C IV and the intercombination lines of C II, C III, and Si III are also quite strong.

b) *Dependence of Emission Spectrum on Model Parameters*

i) *Shock Velocity*

The dependence of optical and UV emission spectra on shock velocity is illustrated by models A–I in Tables 3 and 4. The total Hβ intensity is roughly proportional to the square of the shock velocity if the gas is preionized and all other parameters are kept fixed. At high shock velocities, the ratio of Hα to Hβ decreases because of the high temperature of the recombination zone in fast shocks. The He I 5876 Å line is strongest relative to Hβ in the 80–120 km s^{-1} range, where He II 304 Å is strongest. The He II 4686 Å line increases in strength with increasing shock velocity until all helium ions make a recombination from He III to He II at about 140 km s^{-1}. In faster shocks, increased photoionization increases the number of recombinations made by an average hydrogen atom, while the average helium atom still undergoes only one recombination to He II, so the 4686 Å line becomes weaker relative to Hβ.

The strength of the [O III] lines increases quickly with shock velocity up to about 80 km s^{-1}, at which point oxygen is completely ionized to O III. Faster shocks ionize oxygen to O IV and above, and the absolute strength of the [O III] lines increases slowly for faster shocks. The temperature-sensitive ratio $I(4959+5007)/I(4363)$ decreases smoothly with shock velocity between 50 and 200 km s^{-1}, and would be an excellent velocity indicator where it not made ambiguous by variations in other model parameters.

In slower shocks, [O II] 3727 Å is quite strong, because even at the highest temperatures oxygen is largely O II. The variations of the [O II] $I(3729)/I(3726)$ and [S II] $I(6717)/I(6730)$ ratios result from the higher electron densities due to the larger compression factors in the faster shocks.

ii) *Preshock Density*

Most of the dependence of the flow structure on preshock density is a simple $1/n_0$ scaling of the cooling time and cooling distance. The collisional ionization and recombination rates, as well as the time rate of change of the temperature, are proportional to n_e, so the ionization state at a given temperature is independent of n_0. Since the flux of ionizing radiation produced is proportional to the flux of particles through the shock front, the photoionization rate also scales with the other rates.

The scaling breaks down at low densities and shock velocities ($n_0 v_7^2 < 5$; $v_7 = v/100$ km s^{-1}), when photoionization of elements with ionization potential below 13.6 eV by background starlight becomes important. At high densities, collisional quenching of forbidden lines destroys the proportionality between dT/dt and n_e. If magnetic pressure is negligible, this occurs at $n_0 v_7^2 \approx 4$ for Si II 34.8 μm and $n_0 v_7^2 \approx 150$ for O II 3727 Å. The main effect of quenching of the infrared lines is to lengthen the recombination region and to redistribute the cooling radiation among the infrared lines, but quenching of the optical lines of O II can greatly alter the observed spectrum, both by weakening the O II lines and by enhancing the N II and S II lines which compete for the thermal energy at temperatures near 20,000 K.

iii) *Magnetic Field*

Since the transverse component of the magnetic field is frozen into the gas, the magnetic pressure $B^2/8\pi$ is proportional to the square of the compression factor $x = n/n_0$ and to the square of the magnetic field in the preshock gas. Setting the magnetic pressure equal to the maximum pressure in the postshock region gives an upper limit to the compression (Cox 1970) of

$$x_{\max} = \frac{(P_0 + \rho v_s^2)^{1/2}}{B_0/(8\pi)^{1/2}} .$$

By halting the compression, the magnetic field can affect the flow and emission spectrum by way of the density-dependent mechanisms discussed above. More important, the ionization state in the cooler part of the flow is determined by the competing processes of photoionization and recombination. Since the magnetic field lowers the electron density without changing the flux of ionizing photons, it enhances the relative importance of photoionization. Comparison of models E, P, and Q shows that excitation lines of neutrals are most drastically affected and that lines of singly

ionized species are significantly weakened if the preshock magnetic field is fairly strong.

iv) *Ionization of the Preshock Gas*

The most obvious effect of the preshock ionization state on the flow is the dependence of the postshock temperature on the average ionization energy which the particles bring into the shock. If a significant fraction of the preshock kinetic energy of the flow must be used to ionize the gas, less thermal energy will be available and the postshock temperature will be lower.

The secondary effects are more complicated. The overwhelming abundance of hydrogen and helium compared to other elements implies that even a small amount of neutral hydrogen at $\sim 50{,}000$ K or of He II at $\sim 120{,}000$ K can give large cooling rates. In either case, the radiation spectrum produced by the high-temperature regions of the flow is affected, and therefore the ionization balance in the recombination zone is affected; cooling by hydrogen excitation results in Lyman-line photons, with energies below 13.6 eV, and cooling by He II produces photons above 40 eV, while most other cooling processes produce photons below 25 eV.

The effects of the preshock ionization state can be seen by comparing models E and R, which are identical except that helium flowing into the shock front in the latter model is initially doubly ionized, and by comparing models B and C with models J and K, which are also identical except that the hydrogen and helium flowing into models J and K are 10% and 31% neutral, respectively.

In model E, the gas cools from 150,000 to 50,000 K in about half the time required in model R, in which cooling by helium is small at these temperatures. The longer time spent at high temperatures in the latter case results in stronger [O III] and [Ne III] emission and allows the gas to reach a somewhat higher stage of ionization (30% O IV compared to 23% O IV in model E, for instance). The lines of [O II] are also stronger in model R because He II 304 Å photons keep oxygen doubly ionized to lower temperatures in model E. The emission of neutral carbon, nitrogen, magnesium, and calcium is stronger in the case where cooling by helium is important because the 304 Å photons deposit a large amount of heat for each photoionization; but because they are far above the thresholds of these atoms, they cause relatively few ionizations. Also, because the 304 Å photons preferentially ionize He I rather than H I, the net number of recombinations to the neutral stage of each helium atom passing through the shock front is twice as large if helium is not doubly ionized in the preshock gas. Thus the helium recombination lines in model E are twice as strong as in model R.

The pairs of models B and J, and C and K are analogous to the pair just described, except that, in the lower-velocity shocks, H I is the critical coolant rather than He II. In the flows with the preshock hydrogen 10% neutral, the rapid cooling by excitation of the Lyman lines and the conversion of thermal energy into ionization energy result in a very narrow high-temperature region. This reduces the amount of energy available to the [O II] and [N II] lines and reduces the fraction of oxygen which reaches O^{++}. The strength of the oxygen and nitrogen lines relative to Hβ is further diminished by collisional excitation of Hβ, which enhances the Hβ intensity by 28% in model J and 33% in model K. Since excitation of hydrogen is an effective cooling mechanism below 12,000 K, the absolute strengths of the excitation lines of neutral oxygen, nitrogen, and carbon produced in the recombination zone are not much affected, but some emission in these lines occurs at higher temperatures.

Variations in the preshock ionization state of elements other than hydrogen and helium have less dramatic effects on the flow but can change the optical emission-line strengths considerably. Models L and M illustrate low-velocity shocks which are incapable of collisionally ionizing O^+ to O^{++} but which have the preshock gas in a high state of ionization, 0.31 O^+ and 0.69 O^{++}. This situation is rather likely to arise if the slow shock has evolved from a faster shock, which produced strong He II 304 Å emission and doubly ionized the oxygen in gas ahead of the shock. The recombination time for O^{++} is about $17{,}000/n_e$ years. The excitation rates of both optical and UV radiation of O III are faster than those of O II, and the O III/O II ratios predicted by these models are similar to those produced by a 100 km s^{-1} shock in a less ionized medium. The temperature-sensitive forbidden line ratios [O III] $I(4959+5007)/I(4363)$ and [N II] $I(6548+6584)/I(5755)$ are characteristic of the lower temperatures associated with the slower shocks, however.

v) *Area of the Shock Front*

As described in § II, the area of the shock front determines $R_{\max}$, the cutoff of $E_1(\tau)$ for small τ. The optical spectrum is most sensitive to this parameter if cooling and photoionization by the He II 304 Å line are important.

Models of 100 km s^{-1} shocks with various values of $R_{\max}$ are included in the tables. The large number of photons available in the large-area shocks increase the total number of recombinations undergone by hydrogen, and therefore increases the intensity of Hβ. The increase of He I recombination lines is somewhat larger, but it is partially due to the greater preionization of helium to He II in model E than in model T. The parameter $R_{\max}$ affects photoionization most strongly if τ is small; since photoionization of O II and N II is important mainly at temperatures above 30,000 K, there is little neutral hydrogen or helium to absorb photons produced upstream and $\tau < 0.001$. These ions, and atoms which are photoionized by photons longer than 912 Å, are most sensitive to $R_{\max}$; models with large $R_{\max}$ generally show relatively weak [O II], Mg I], [C I], and [Ca I] emission. The photoionization of O II and N II also means that more of the oxygen and nitrogen at $\sim 40{,}000$ K is doubly ionized, so models with high values of $R_{\max}$ generally

have [O III] and [N II] temperature-sensitive line ratios indicative of relatively low temperatures. A large value of R_{max} also tends to increase the temperature and extent of the recombination zone, resulting in stronger [O I] and [N I] emission.

vi) *Abundances*

The calculations assume that elemental abundances are constant through the shock and cooling region—i.e., no molecules are formed—and that any destruction of grains occurs in the shock front itself. It is certainly possible that some sputtering of grains occurs in the hot regions of the flow, but the rates are highly uncertain. Grains composed of graphite or silicates could probably survive even the highest temperatures produced in a 200 km s^{-1} shock (Silk and Burke 1974; Burke and Silk 1974). Thus, if sputtering occurred during the course of the flow, the main effect would be the slow addition of the icy components of grains to the hot regions of the flow. This might mean larger amounts of O II and N II in the high-temperature areas and an enhancement of the optical lines of these ions. It is also possible that grain-grain collisions are important, as the grains, with a charge of about 100 electron charges, have their bulk motion ahead of the shock converted into circular motion about the magnetic field behind the shock (Jura 1976).

Since the rates for processes which destroy grains are quite uncertain, various extreme cases were chosen, corresponding to (set A) no depletion (Allen 1973), (set G) depletion of the interstellar medium as estimated by Spitzer and Jenkins (1975), and (set G1) survival of graphite and silicate grains but not of ices. These sets of abundances are listed in Table 2, along with sets of abundances chosen to match observations of the Cygnus Loop (Miller 1974). One model was run with abundances derived for the Magellenic Clouds by Dufour (1975) and Fry and Aller (1975). This set of abundances predicts extremely weak lines of nitrogen and neon compared to observations of N49 by Osterbrock and Dufour (1973). Dopita (1976) suggests that the difference in apparent abundances between shocks and H II regions in the LMC could result from destruction of grains in the shock waves. No model was run with sputtering in the cooling region, which differs qualitatively because of the delayed source function of heavy elements.

The depletion by condensation onto grains of nonvolatile elements (all but He, N, O, and Ne) weakens the lines of Mg, Ca, and Fe more or less in proportion to their depletion. The depletion of carbon and silicon enhances the intensities of lines of other elements by decreasing the cooling rate and the share of the energy taken by C and Si lines. Models in which abundance set G1 is assumed show lines of O II and N II about twice as strong as do models with set A. Removal of carbon and silicon also enhances the O III lines by about 50% and even increases the intensity of the S II lines by 30%, although sulfur is depleted by a factor of 2 in set G1. The dependence of the spectra on the abundances can be seen by comparing model E with models U and V at 100 km s^{-1}, or with models C and BB at 70 km s^{-1}.

c) *Accuracy*

The accuracy of the models is limited mainly by the accuracy of the atomic rates used and by the approximations to the flow and radiative transfer equations. The errors due to the finite step size of the computer calculations were estimated by comparing models with very large and very small steps, and should be less than 10%; the largest uncertainties occur in lines of neutrals other than hydrogen and helium.

The accuracy of a given atomic rate is roughly proportional to its importance; quite reliable rates are available for excitation of the forbidden lines of oxygen and nitrogen and for most of the UV lines important for cooling. Ionization and recombination rates for elements other than calcium and iron should also be fairly accurate. As a check on the sensitivity of the results to uncertainty of the ionization and recombination rates, a model was run with the correction factor which Burgess and Tworkowski (1976) suggest for dielectronic recombination to helium-like ions applied to all ions. For the most part, this changed the optical spectrum by less than 10%; but the strength of [O II] λ3727 is rather sensitive to the temperature at which O III recombines to O II, and the O II lines were lower by nearly 30% in the model with the helium-like correction applied to other ions.

The main approximations to the flow equations, the assumption that $T_e = T_i$, the assumption of instantaneous thermalization of the flow velocity in the shock front, and the assumption that thermal conduction is negligible may result in substantial inaccuracy in the flow very near the shock front but should have little effect on the optical emission spectrum. The rough treatment of radiative transfer is probably not a major source of error except in shocks in which photoionization by He II 304 Å photons is important. The estimates of the effects of resonant scattering on this line made in § II indicate that such scattering may reduce the photoionization rates due to this line by as much as 30%. This might be partially taken into account by choosing a smaller value of R_{max} than would be estimated from the geometry of the flow. As an extreme case, a model was run with the 304 Å line removed from the downstream traveling radiation. Comparison of this model to the others indicates that the approximate treatment of radiative transfer for this line introduces a 10% uncertainty to the lines of singly ionized species and a slightly greater uncertainty to the lines of neutrals; but much smaller errors are likely in models with small values of R_{max}, preionization of helium to He III, or velocities outside the 80–120 km s^{-1} range in which this line is most important. As mentioned in § II, the approximate treatment of the summations in the ionization rates introduces a 10% uncertainty.

d) *Stability*

Two recent papers have pointed out that instabilities occur in the radiatively cooling flow behind a shock front if density perturbations are present in the preshock gas. McCray, Stein, and Kafatos (1975) consider thermal instabilities due to the binary nature of the cooling. Since the cooling rate is proportional to $n_e n(\mathrm{H})$ while the thermal energy content of the gas is proportional to $n(\mathrm{H})$, a region of higher density will cool faster, resulting in further compression and still faster cooling unless the cooling rate decreases quickly enough with temperature to stabilize the flow. The calculations of McCray *et al.* indicate that the flow behind a plane-parallel shock is unstable if $d(\ln L)/d(\ln T) < 3$.

The cooling rates for a few models are shown in Figures 1–3. Unless helium is largely doubly ionized in the preshock gas, $d(\ln L)/d(\ln T) \approx 3$ for shocks between 80 and 120 km s^{-1}. In the 140 km s^{-1} models, $d(\ln L)/d(\ln T)$ is between 4 and 5 above 120,000 K, making the flow stable for about half the cooling distance and limiting the density enhancement to be expected from instabilities. Chevalier and Theys (1975) consider an oblique shock at the edge of a density perturbation; while they do not give a criterion for stability, the density perturbation is probably not enhanced if $d(\ln L)/d(\ln T) \geq 3$.

The present models point to a possible enhancement of these instabilities, however, since the ionization state of the preshock gas can have major effects on the cooling rate. Whether the gas is slowly recombining (after being ionized by the supernova itself or by faster shocks at an earlier phase of the supernova remnant's history) or the ionization state of the preshock gas is determined by the balance of photoionization and collisional recombination rates, the ionization state in denser regions of the preshock gas will be lower. In cases in which cooling by He II is important, the fraction of He II would be larger in the dense regions and the cooling rates in the postshock gas would be larger. By itself, this mechanism could produce density enhancements by only a factor of 2 or so, because the difference in cooling rates disappears by the time the gas cools to around 40,000 K; but it could make other types of instability more effective.

If these instabilities are important, one would expect to see emission mainly from the denser regions, which would be experiencing the less intense radiation from the more diffuse neighboring parts of the flow, so a shock with such instabilities should look like a shock with higher n_0 than the actual average n_0 with an unusually weak radiation field. This could be roughly taken into account by choosing a lower value for $R_{\max}$.

V. INTERPRETATION OF OPTICAL SPECTRA

a) *General Methods*

The dependence of the optical spectrum of a shock on shock parameters is sufficiently complex that there seems to be no simple method for methodically determining the shock conditions from observed intensities. Dopita (1977) has calculated diagnostic diagrams which are a step toward such a method, but without considering magnetic field, shock-front area, or the effects of variations in the preshock ionization state. The present models agree reasonably well with his diagrams for determination of abundances but less well with those relating to postshock temperature. Model CC duplicates the parameters of Dopita's reference model. This subsection will consider what limited information can be drawn unambiguously from the intensities of the important optical lines, and the following subsections will deal with specific examples.

The prominent optical lines of hydrogen are Hα and Hβ. The intensity of Hβ is proportional to n_0 and roughly proportional to v_s^2 (see models A–I), so a measurement of the absolute intensity of Hβ could give an estimate of $n_0 v_s^2$. Usually, only the ratio $I(\mathrm{H}\alpha)/I(\mathrm{H}\beta)$ is accurately known, however. In most models, this ratio falls between 2.9 and 3.3, with the lower values occurring in fast shocks.

The optical lines of helium are produced mainly by recombination. If $N(\mathrm{He})/N(\mathrm{H}) = 0.085$ and $I(5876)/I(\mathrm{H}\beta) > 0.13$, the average helium atom recombines more often than does the average hydrogen atom. This generally means that photoionization of He^0 by He II 304 Å photons is important, and it indicates a shock velocity between 80 and 120 km s^{-1} and preshock helium that is predominantly neutral or singly ionized. The He I 5876 Å line is significantly weaker than $0.13 \times I(\mathrm{H}\beta)$ in slow shocks, in which helium never becomes fully ionized, and in fast shocks, in which hydrogen is photoionized many times.

In shocks with $n_0 \lesssim 10$ cm^{-3}, the He I 10830 Å line is produced by recombination and is typically less than $0.4 \times I(\mathrm{H}\beta)$. For higher values of n_0, excitations from the metastable level of He I enhance this line, and models Z and AA, which have electron densities of 9000 and 11,000 cm^{-3} in the helium recombination region, have He I 10830 Å intensities 1.52 and 2.57 times the Hβ intensity.

In all the models presented here, each He^{+2} ion recombines once, so the intensity of He II 4686 Å provides an estimate of the maximum ionization fraction of He^{+2}. Again assuming $N(\mathrm{He})/N(\mathrm{H}) = 0.085$, the maximum ionization fraction of He^{+2} is found to be about $10/v_7 \times I(4686)/I(\mathrm{H}\beta)$.

The [C I] lines at 9823 and 9850 Å are indicators of the carbon abundance and conditions in the recombination zone. Unfortunately, v_s, n_0, B_0, and $R_{\max}$ all influence the ratio of the C I photoionization rate to the C II recombination rate and the temperature of the region in which C I is found. Furthermore, the [C I] collision strengths used are only estimates, so the [C I] intensities listed in Table 3 should not be taken too seriously. The general trends of the predicted intensities should be correct, however. The 9823 and 9850 Å lines are most intense in moderately high density, low magnetic field shocks, since these conditions favor a high C I ionization fraction. For

instance, model Q, which has $B_0 = 10\ \mu$gauss, produces [C I] lines one-fifth as intense as model P, which is identical except for a low magnetic field, 0.1 μgauss. Because the C I forbidden lines are sensitive to the temperature and extent of the recombination region, they are strong in models E–G; but in models H and I, collisional quenching ($N_{crit} \approx 2 \times 10^4\ cm^{-3}$ for the value of Ω used) weakens the [C I] lines.

The optical forbidden lines of N I and N II are less sensitive to the parameters associated with photoionization than are the [C I] lines. As with most other excitation lines of neutrals, [N I] 5200 Å is strongest in shocks which have a long, high-temperature recombination zone. If the intensity of [N I] 5200 Å is greater than about 0.3 × $I(H\beta)$, carbon and silicon are probably depleted relative to nitrogen.

A plot of the ratio I(N II 6548–6584)/I(O II 3727) against I(N I 5200)/I(O I 6300–6363) is shown in Figure 4. Collisional quenching at high densities makes these ratios ambiguous, but at moderate densities they are indicative of the ratio of oxygen and nitrogen abundances (models CC, DD, EE, and GG). The increase in the intensities of the [N II] lines compared to the [O II] lines as the shock velocity increases is a result of collisional de-excitation of the [O II] lines at the higher densities produced by the faster shocks and of increased [N II] emission in the more extensive recombination zones of these shocks. The [N II] emission from the recombination zone is also responsible for the change in the temperature-sensitive ratio I(6548–6584)/I(5755) plotted with the temperature-sensitive ratio of [O III] lines in Figure 6. In these plots, the solid lines connect models which are similar except for shock velocity. Points labeled 1, 2, and 3 refer to measurements made by Miller (1974) at three positions in the Cygnus Loop, and HH 1 refers to measurements of that Herbig-Haro object made by Böhm, Siegmund, and Schwartz (1976). Figure 5 also includes a few points to indicate the effects of doubly ionized helium in the preshock gas (model R) or a low value of R_{max} (model S).

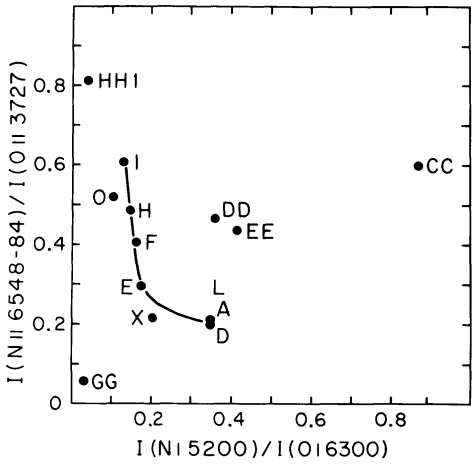

FIG. 4.—Ratios of nitrogen forbidden line intensities to oxygen forbidden line intensities.

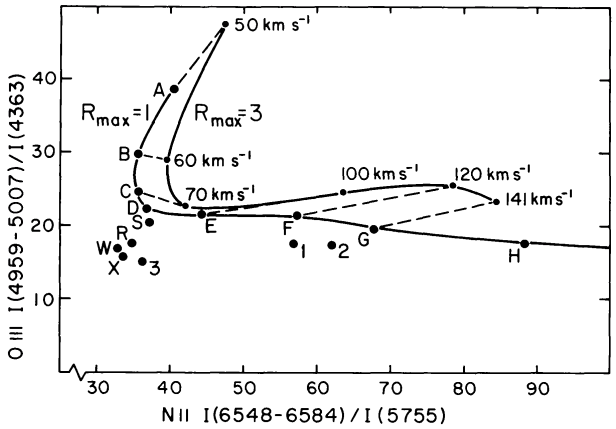

FIG. 5.—Temperature-sensitive line ratios of [O III] and [N II].

The forbidden lines of oxygen are generally the strongest optical lines; since the atomic rates used for oxygen are probably more accurate than are those for most other elements, the oxygen lines should be the most reliable indicators of shock parameters. The ratios of [O II] 3727 Å and [O I] 6300 Å to [O III] 5007 Å (Fig. 6) give an estimate of the shock velocity, but the I(6300)/I(5007) ratio is rather sensitive to depletion of carbon and silicon (models U, V, and BB). The ratio of [O III] 5007 Å to Hβ is sensitive to shock velocity, since shocks slower than 70 km s^{-1} cannot doubly ionize oxygen while those faster than 140 km s^{-1} produce so much Hβ that the oxygen line becomes relatively weak. However, if some oxygen is doubly ionized in the preshock gas, even a very slow shock can produce strong [O III] lines (models L and M). Depletion of carbon or silicon relative to oxygen or double ionization of helium in the preshock gas can slow the cooling in the high-temperature region and

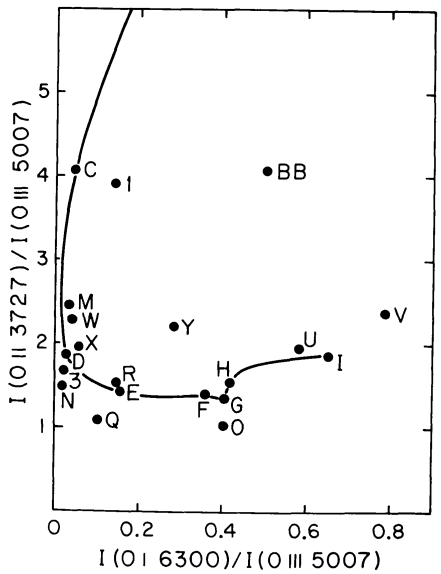

FIG. 6.—Line intensity ratios of [O II] to [O III] and [O I] to [O III].

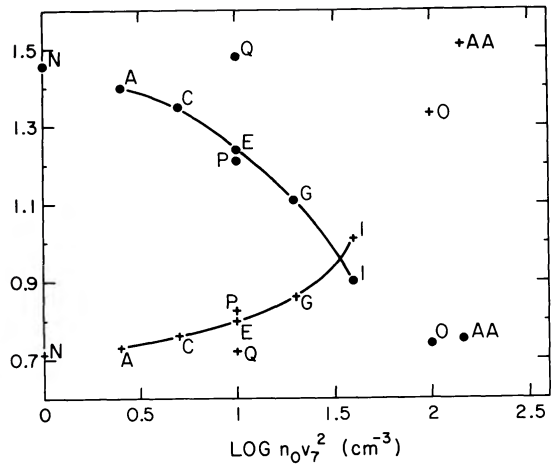

FIG. 7.—Density-sensitive ratios of (*dots*) [O II] $I(3729)/I(3726)$ and (*pluses*) [S II] $I(6730)/I(6717)$.

strengthen the [O III] lines considerably (models U, V, and R). If the temperature-sensitive ratio of [O III] lines, $I(4959+5007)/I(4363)$, is less than about 17, the high-temperature zone must be rather long, and depletion of carbon and silicon or preionization of helium to He^{+2} is likely. If this ratio is greater than 25 or 30, [O III] emission occurs at fairly low temperatures, indicating a slow shock.

The [O II] $I(3729)/I(3726)$ ratio is primarily sensitive to electron density, which in turn depends on the preshock density and on the compression achieved. Figure 7 plots this ratio and $I(6730)/I(6717)$ of [S II] lines against $n_0v_7^2$, but models P and O show how sensitive these ratios are to magnetic field. The temperature-sensitive ratio of [O II], $I(7320–7330)/I(4363)$, shows remarkably little variation with shock velocity (models B–I). This is partly because the [O II] emission is very sharply peaked at about 20,000 K; but it is partly fortuitous, since [O II] emission in the extended recombination zones of the faster shocks at temperatures around 7500 K produces very little emission in the 7320–7330 Å lines, but this balances the relatively high intensities of these lines produced at higher temperatures due to ^2D–^2P excitation and ^2D–^4S de-excitation. The $I(7320–7330)/I(3727)$ ratio is smaller than 0.03 in low-velocity or low-density shocks (models A, J, and N) and higher than 0.04 in high-density flows (model O).

The only optical lines of neon are the [Ne III] lines at 3868 and 3967 Å. Like I(O III 5007)/$I(H\beta)$, the ratio of [Ne III] 3868 Å to $H\beta$ peaks at velocities near 100 km s^{-1} and is sensitive to depletion of carbon and silicon and to the initial ionization state of the gas. The ratio $I(3868)/I(5007)$ is less sensitive to these parameters, and in most cases the abundance ratio $N(\mathrm{Ne})/N(\mathrm{O}) = (1.35 \pm 0.20)I(3868)/I(5007)$. The ionization potential of Ne^+ is higher than that of O^+, however; in very slow shocks or in shocks in which photoionization of O^+ by He II 304 Å photons is important, this formula may underestimate the neon abundance. In very fast shocks, [Ne V] lines are produced. In models H and I, $I(3346+3426)/I(H\beta) =$ 0.058 and 0.24.

The only ion of sulfur having strong optical lines is S II, but the lines of S I and S III in the near-infrared may also be observable. The forbidden lines of S I were not included in the models because no collision strengths are available, but the similarities in energy levels and ionization potentials between C I and S I suggest that the ratio of S I 10819 Å to the C I line at 9850 Å will be about the ratio of sulfur abundance to carbon abundance.

The [S II] lines at 6717–6730 Å and 4067–4076 Å give density and temperature estimates analogous to those of the [O II] lines, but the collision strengths are somewhat less certain. The values of Ω given by Krueger and Czyzak (1970) multiplied by a factor of 1.8 below the ^4S–^2P threshold as suggested by Saraph and Seaton (1970) predict line intensities which are in reasonable agreement with the Cygnus Loop observations of Miller (1974) and are close to the values given by Pradhan (1976). As a result of the lower excitation energies and higher critical densities of the [S II] lines compared to the [O II] lines, and also as a result of the lower ionization potentials of S I and S II as compared to those of O I and O II, the [S II] lines are emitted, on the average, at lower T_e and higher n_e than are the [O II] lines. In model EE, for instance, the average electron density at which the [O II] lines are emitted, defined as $\langle n_eP_\lambda n_en(\mathrm{H})\rangle/\langle P_\lambda n_en(\mathrm{H})\rangle$, is 337 cm^{-3}, while the average density for the [S II] lines is 514. The difference diminishes in faster shocks as more [O II] emission comes from the extended recombination zone.

The optical lines of calcium are the resonance lines Ca I 4227 Å and Ca II 3934–3968 Å and the forbidden $4s$–$3d$ transitions at 7291 and 7324 Å. All these lines are too weak to be observed if calcium is condensed onto grains by the amount suggested by Spitzer and Jenkins (1975). Thus detection of any of these lines indicates an undepleted preshock gas or partial destruction of the grains in the shock. Like the [C I] and Mg I] lines, the Ca I line requires a high enough electron density that recombination of Ca^+ can overcome photoionization of neutral calcium. Interpretation of the Ca II lines is complicated by the possibility that resonant scattering of $4p \rightarrow 4s'$ 3945 Å photons eventually converts them into $4p \rightarrow 3d$ and $3d \rightarrow 4s$ photons. Since the branching ratio for this process is 0.067 and since the optical depth for the resonance line photons through the shock and cooling region is less than 1 in all models given here, this process is ignored in the calculations. If conversion of resonance line photons to forbidden line photons is important, the $4p \rightarrow 3d$ lines at 8498 and 8542 Å should be comparable to the 7291 Å line.

Optical lines of Fe II, Fe III, and Fe V are seen in supernova remnants, but reliable collision strengths are available only for Fe III. The strongest line, $^3F_4 \rightarrow {}^5D_4$ 4658 Å, is listed in Table 3. The [Fe III] 5272 and 4703 Å lines are about one-third as strong in all models run, and are useful as diagnostics only at higher densities than those assumed. If the ratio

$I(4658)/I(5007)$ is less than about 0.08, depletion of iron relative to oxygen is likely, while if this ratio is greater than 0.2, the shock is probably slow enough that double ionization of oxygen does not proceed to completion.

b) The Cygnus Loop

The optical filaments of the Cygnus Loop are generally believed to be the result of shock waves associated with a fairly old supernova remnant (Cox 1972*a*). The Cygnus Loop is also a source of X-ray and radio emission (e.g., Rappaport *et al.* 1974; deNoyer 1974). The X-ray spectrum and the detection of the Fe XIV 5303 Å line (Woodgate *et al.* 1974) indicate that the X-rays are produced by gas at 2×10^6 K. Such gas is produced by shock waves moving at 300–400 km s^{-1}; but at the densities of around 1 cm^{-3} which account for the X-ray emission, this gas would require over 10^5 years to cool sufficiently to produce the observed optical lines. Since this is at least 4 times the age of the remnant (e.g., Rappaport *et al.* 1974), the optical filaments cannot be formed by thermally unstable cooling of the hot gas. It therefore seems likely that the optical filaments result from higher-density material encountered by the shock. Roughly the same ram pressure is required to drive a shock at 100 km s^{-1} into a gas with $n_0 = 10$ cm^{-3} as is required to drive a 300–400 km s^{-1} shock into a gas with $n_0 = 0.5$–1 cm^{-3}. On the basis of the X-ray flux (Rappaport *et al.* 1974) and a distance of 800 pc, the ionization rates due to X-rays are less than 10^{-13} s^{-1} and may be neglected. Photoionization by EUV photons will be somewhat faster, but if the temperature given by Rappaport *et al.* for the X-ray spectrum is characteristic of most of the emitting gas, the spectral calculations of Raymond and Smith (1977) indicate that this may also be neglected. The pressure of the relativistic electrons responsible for the radio emission should behave like magnetic field pressure and ought to be included in B_0.

Detailed observations of the optical spectrum of the Cygnus Loop have been made by Miller (1974) at three positions. Miller's stated error limits are 10% for lines stronger than Hβ, 25% for lines more than one-tenth as strong as Hβ, and up to 50% for weaker lines. Thus the uncertainties in the temperature-sensitive ratios are appreciable, particularly in that of [N II]. At a distance of 800 pc, the 2".7 wide slit used for the measurements should include the entire cooling region behind a shock, but more than one shock may fall within the aperture. With these difficulties in mind, we try to match a model to the observations. It is interesting that models with $R_{max} = 1.0$ match the observations better than those with $R_{max} = 3.0$, indicating that the radiative transfer is characteristic of individual filaments rather than of the Cygnus Loop as a whole.

Table 6 lists Miller's (1974) observations, the predictions of Cox's (1972*a*) models, and those of three of the present models. The spectra at positions 1 and 2 are seen to be fairly similar but markedly different from that at position 3. A clue to the cause of this difference lies in the intensities of the helium recombination lines; He II 4686 Å is twice as strong relative to Hβ at position 3 as at the other two positions, while He I 5876 Å is half as strong. This suggests that helium is doubly ionized in the preshock gas at position 3 but not at the other positions. The stronger He I line at positions 1 and 2 then results from recombinations following photoionizations of neutral helium by He II 304 Å photons. This difference in the preshock ionization state also explains the relatively great strength of the [O III] and [Ne III] lines at position 3 as being due to the lack of cooling by helium in the high-temperature region. This is also the cause of the low value of the $I(4959+5007)/I(4363)$ ratio, since a larger fraction of the [O III] emission is produced at high temperatures.

The strong oxygen, nitrogen, and sulfur forbidden lines require a higher abundance of these elements relative to carbon and silicon compared to the Allen

TABLE 6

COMPARISON OF MODELS WITH CYGNUS LOOP OBSERVATIONS

Ions	Lines	Observations (Miller1974)			Models (Cox 1972*a*)		Present Models		
		1	2	3	71 km s^{-1}	141 km s^{-1}	W	X	YY
O III.....	(4959+5007)/4363	17.5	17.1	14.8	25	16	16.8	15.6	18.2
N II.....	(6548+6584)/5755	58.6	61.9	36.3	69	176	32.7	33.7	37.2
O II.....	(7320–7330)/3727	0.040	0.037	0.047	0.048	0.030	0.036	0.038	0.037
S II.....	(6717–6730)/(4067–4076)	14.5	12.3	10.4	...	...	10.3	10.3	12.7
O II.....	3729/3726	1.25	1.40	1.31	1.42	1.32	1.32	1.26	1.26
S II.....	6730/6717	0.84	0.76	0.88	...	...	0.78	0.81	0.78
O III, H....	5007/Hβ	3.32	2.52	9.50	3.1	2.3	6.53	6.61	6.16
O II, H.....	3727/Hβ	13.0	12.8	15.9	14.5	10.2	15.0	12.6	13.5
O I, H.....	6300/Hβ	0.47	...	0.20	0.21	0.76	0.27	0.38	1.76
N II, H.....	6584/Hα	0.83	0.87	0.84	1.12	1.07	0.74	0.66	0.80
S II, H.....	(6717–6730)/Hα	0.92	1.26	0.78	...	...	1.01	0.91	0.38
Ne III, H...	3869/Hβ	0.80	...	1.68	0.97	1.07	1.40	1.33	0.65
He I, H....	5876/Hβ	0.10	0.093	0.056	0.19	0.076	0.088	0.085	0.14
He II, H....	4686/Hβ	0.042	0.048	0.092	...	...	0.12	0.11	0.059
O II, O III....	3727/5007	3.92	5.08	1.67	2.75	2.52	2.29	1.90	2.19
O I, O III...	6300/5007	0.14	...	0.02	0.09	0.33	0.041	0.057	0.29

(1973) cosmic abundances. Lines of Ca II and Mg I which Miller identified in his photographic spectra but did not measure (his Fig. 2) indicate that, if condensation onto grains is responsible for depletion of carbon and silicon, this depletion is less severe than predicted by standard grain depletion models (Spitzer and Jenkins 1975). This may mean that some grains are destroyed by the shock.

The strong [Ne III] line indicates that the abundance ratio $N(\mathrm{Ne})/N(\mathrm{O})$ is about 0.25, or twice the cosmic abundance. The sulfur lines also appear to require an overabundance of sulfur by about a factor of 2, while the cosmic nitrogen to oxygen abundance ratio appears correct. This is roughly what one would expect from partial condensation of heavy elements onto grains, since neon would be undepleted and sulfur would be somewhat less depleted than oxygen or nitrogen. However, any depletion of oxygen would weaken the [O II] lines relative to Hβ, since cooling by Lα would take a larger fraction of the energy at temperatures near 20,000 K. It seems more likely, therefore, that neon and sulfur are overabundant.

As discussed in § IV*b*, it is difficult to disentangle n_0 from B_0. Models in which compression is limited by the magnetic field seem less likely to show the greater electron density as derived from the S II lines compared to that derived from the [O III] lines seen here, however, and generally seem to have very weak Mg I lines and lower values of the ratio $I(3727)/I(5007)$, so it is reasonable to assume that the magnetic field is unimportant. Model X, a 100 km s^{-1} shock with $n_0 = 10\ \mathrm{cm}^{-3}$ and a very small magnetic field, matches the [O II] $I(3719)/I(3726)$ and [S II] $I(6730)/I(6717)$ ratios measured at position 1 quite well, but position 3 seems to require a lower density for the [O II] lines and a higher one for the [S II] lines. The rather high $I(7320\text{–}7330)I(3727)$ and low $I(6717\text{–}6730)/I(4074)$ ratios indicate that the density at position 3 may be somewhat higher than at position 1.

The spectrum at position 3 matches a shock at 80–100 km s^{-1} reasonably well if carbon and silicon are depleted with respect to oxygen, though not necessarily as drastically as assumed in models X, Y, and W, and if helium is mostly doubly ionized in the preshock gas. The preshock density is apparently about 10 cm^{-3}, and the magnetic field seems to be small. The only serious discrepancy between these models and the observations is the $I(5007)/I(\mathrm{H}\beta)$ ratio. None of the models that were run predicted an intensity of [O III] 5007 Å as large as 9 times the Hβ intensity. It is possible that the [O III] emission peaks sharply at 90 km s^{-1}, but it seems more likely that larger photoionization rates for O^+ due to a larger value of $R_{\max}$ or that the presence of a small amount of He^+ in the preshock gas would increase the strength of the 5007 Å line above the model predictions.

An alternative possibility is that the postshock flow at position 3 is thermally unstable. As mentioned in § IV*d*, shocks at about 100 km s^{-1} with neutral or single ionized helium in the preshock gas are stable, while those with preshock helium doubly ionized are thermally unstable (McCray *et al.*; Chevalier and Theys 1975). It was found above that helium is doubly ionized ahead of the shock at position 3, so chance enhancement of the emission from $T \approx 20{,}000$ K due to the instability could account for the strength of [O II] and [O III] lines. This instability might also account for the apparent discrepancy between electron densities obtained from [O II] and [S II] line ratios.

The matching of models to positions 1 and 2 is somewhat more ambiguous than the matching at position 3, but the ratios of [O II] to [O III] lines indicate a shock at about 70 km s^{-1} with some depletion of carbon and silicon (Fig. 6). About one-third of the helium in the preshock gas must be doubly ionized to account for the intensity of the He II line, and the density of the preshock gas at position 1 must be 10–20 cm^{-3}, while position 2 requires either $n_0 \approx 5\ \mathrm{cm}^{-3}$ or $B_0 \approx 5\ \mu$gauss. The [N II] line ratio indicates a faster shock (Fig. 6), but the shock velocities near 120 km s^{-1} which produce $I(6548+6584)/I(5755) \approx 60$ give too much [O I] and too little [O II] emission compared to [O III] to match the measurements. It is possible that the combination of depletion of carbon and silicon and partial double ionization of the preshock helium slows the cooling in the high-temperature region enough to allow nitrogen to become doubly ionized, decreasing the [N II] emission at high temperatures and increasing the $I(6548+6584)/I(5755)$ ratio. The abundances found for position 3 are consistent with the spectra of positions 1 and 2, but the overabundance of neon and sulfur need not be as high.

c) The Vela Supernova Remnant

Optical spectra of a filament of this supernova remnant have been published by Milne (1968) and Osterbrock and Costero (1973). Comparing standard abundance models with the latter measurement, we find that a shock slow enough to give the correct $I([\mathrm{O\ III}]\ 5007)/I(\mathrm{H}\beta)$ predicts too much [O II] λ3727 and too little [O I] λ6300 by factors of 2, while a shock at ~100 km s^{-1} gives the observed [O I] and [O II] intensities but too much [O III] by a factor of 5. A shock at about 70 km s^{-1} with depleted abundances gives reasonable intensities for the lines of hydrogen, helium, and oxygen but requires that nitrogen and sulfur be undepleted to match the lines of those elements.

Column densities of various ions in high-velocity gas presumably associated with the Vela supernova remnant have been measured by Jenkins *et al.* The −180 and −90 km s^{-1} components seen against HD 74455 and HD 75821, respectively, are probably cooling postshock gas, but comparison with models is difficult because the angle between the line of sight and the flow direction is unknown and because the assumption of steady flow appears to be in appropriate.

The column densities listed in Table 10 of Jenkins *et al.* for the higher stages of ionization in the −180 km s^{-1} component are in reasonable agreement with models of 160–180 km s^{-1} shocks, but the models

predict far too much O I and N I. The -90 km s^{-1} gas contains O VI, implying either a shock faster than 150 km s^{-1} seen at an angle or significant ionization by X-rays on cosmic rays associated with the supernova remnant. In either case, the models predict too much N I and O I. For both the -180 and -90 km s^{-1} gas, the small observed amounts of low stages of ionization indicate that the cooling does not proceed beyond about 10^4 K. One possible explanation is that the observed gas was reached by the supernova blast wave only about $1000/n_0$ years ago, so that a steady flow pattern has not yet been established. Another possibility is that the supernova remnant itself is now making the transition from adiabatic blast wave to the expanding cold shell (snowplow) phase. The calculations of Cox (1972*b*) and Chevalier (1974) indicate that this occurs as the expansion velocity of the remnant slows to ~ 150 km s^{-1}.

d) Herbig-Haro Objects

Various models have been proposed to explain the emission from Herbig-Haro (HH) objects, but recent observations of emission-line spectra and radial velocities (Böhm *et al.*; Schwartz 1976; Münch 1977) give support to the hypothesis that some HH objects are shock waves driven by the wind of an unseen protostar (Osterbrock 1958; Schwartz 1975), while polarization measurements (Strom, Strom, and Kinman 1974) show that other HH objects are probably reflection nebulae. Comparison of the shock wave models with the spectra obtained by Böhm *et al.* and Schwartz (1976) shows that shocks at velocities of ~ 70 km s^{-1} in gas with a preshock density of ~ 300 cm^{-3} can account for most of the observed features of the spectra. The agreement is less satisfactory than that obtained for the Cygnus Loop for several reasons. Böhm *et al.* express doubt about the applicability of standard reddening corrections for these objects. If the shocks are bow shocks in a wind striking a small cloud, the plane-parallel flow assumed is a poor approximation (Schwartz 1977) and the assumption of steady flow is also poor, since some HH objects are observed to change in times of about 10 years, which is roughly the same as the cooling time of postshock gas in the models. Furthermore, the models with substantial neutral hydrogen fractions in the preshock gas are less accurate than the model of shocks in fully ionized gas.

Table 7 lists the observed line intensities for two HH objects with predicted intensities from two of the models, model FF with $v_0 = 70$ km s^{-1}, $n_0 = 300$ cm^{-3}, cosmic abundances, and preshock gas 20% neutral, and model HH with depleted abundances and ionized preshock gas. Model HH predicts [O II] and [O III] lines too intense, while model FF gives [C I] too strong and [S II] too weak. Odd abundances due to selective destruction of grains may account for the latter, and shocks with parameters similar to those of the models are plausible candidates for these HH objects. The observed intensity ratio I(He I 10820)/I(Hβ) > 1.0 is due to population of the metastable $1s2s\ ^3S$ level by recombinations and excitation from that level to $1s2p\ ^3P$.

A few lines are far from the predictions of either model. The [Ca II] λ7291 line is much stronger than predicted. Repeated scatterings of the resonance lines could enhance this line but would also produce $4p \rightarrow 3d$ lines of comparable intensity. The high intensities observed for λ7291 seem incompatible with the lower intensities of the blend of [Ca II] λ7324 with

TABLE 7

HERBIG-HARO OBJECTS

	BOHM ET AL.			SCHWARTZ		MODEL	
LINE	HH 1	HH 2H	HH 2G	HH 1 SE	HH 1 NW	FF	HH
[O II] λ3727	186.1	199.7	237.7	294.	254.	240.	429.
[Ne III] λ3869	12.2	9.4	24.3	...	...	0.35	54.
Ca II λ3934	12.0	11.8	...	32.	23.	9.6	...
[S II] λ4073	68.8	41.5	50.3	64.	70.	8.7	26.3
[Mg I] λ4571	9.9	11.9	...	15.	10.	8.0	2.8
[Fe III] λ4658	27.8	11.0	...	...	...	...	27.2
Hβ	100.	100.	100.	100.	100.	100.	100.
[O III] λ5007	39.4	88.3	53.7	38.	36.	33.	157.
[N I] λ5200	4.5	8.4	...	50.	17.	1.5	8.2
[N II] λ5755	3.	5.1	...	12.	5.	2.5	3.3
He I λ5876	7.2	...	...	...	7.	5.4	11.
[O I] λ6300	115.3	112.3	...	...	171.	44.	99.
Hα	265.8	330.7	486.8	...	363.	...	300.
[N II] λ6584	114.2	170.8	35.8	...	164.	131.	89.
[S II] λ6717	82.7	27.2	15.5	...	61.	13.9	70.
[S II] λ6730	107.8	39.8	...	...	111.	3.9	96.
[Ca II] λ7291	29.1	23.7	49.5	...	...	1.5	...
[O II] λ7320	...	...	...	...	...	...	...
[Ca II] λ7324	9.9	46.5	13.9	...	...	23.	39.
[O II] λ7330	...	...	...	...	...	...	...
[C I] λ9849	...	11.3	...	...	...	120.	98.
[S II] λ10330	22.2	13.7	...	...	...	4.7	14.
He I λ10830	133.2	147.4	458.6	...	...	164.	...

[O II] λλ7230–7230 in HH 1 and HH 2G. The [C I] line is much stronger in the models than in the observed spectra. While the atomic rates for this line are uncertain, it seems likely that carbon is more severely depleted than assumed in model HH.

The high intensities of the [O I] and [N I] lines obtained by Schwartz (1976) present a more serious problem. The removal of carbon as a coolant would enhance the [N I] and [O I] lines possibly enough to give agreement with the northwest portion of HH 1, but the value $I([\mathrm{N\ I}])/I(\mathrm{H}\beta) = 0.5$ obtained for the southeast region is given only by models of faster shocks which produce too much [O III] emission.

The most likely explanation is a departure from a steady flow, planar shock (Schwartz 1977; Dopita 1978). Another possibility is suggested by the model of Schwartz (1977), in which the optical emission is produced by a bow shock as a wind from a protostar encounters a small cloud. This model also predicts a slower shock, $v_s \approx 10\ \mathrm{km\ s^{-1}}$, driven into the cloud. Combinations of v_s and preshock temperature which produce postshock temperatures ~ 9000 K produce strong lines of [N I] and [O I]. From the pressure balance condition

$$n_0 v_s^2|_{\mathrm{cloud}} \approx n_0 v_s^2|_{\mathrm{wind}}$$

and the assumptions

$$v_s|_{\mathrm{cloud}} \approx 10\ \mathrm{km\ s^{-1}},$$

$$v_s|_{\mathrm{wind}} \approx 70\ \mathrm{km\ s^{-1}},$$

it appears that the cloud shock could produce [O I] and [N I] radiation several times as intense as that produced by the bow shock. Since the emission of the cloud shock is quite sensitive to the ratio of cloud and wind densities, it would vary greatly from one HH condensation to another.

VI. CONCLUSIONS

The shock wave models presented here provide a means of interpreting optical and UV spectra of shock waves in the interstellar medium. The models fit observations of the optical filaments of the Cygnus Loop and the Vela supernova remnant; but because the assumptions of steady, plane-parallel flow break down, the models give only a rough fit to observations of the ion column densities in high-velocity gas in the Vela supernova remnant and to optical spectra of Herbig-Haro objects.

The author thanks Don Cox for suggesting this project and for continued help, and B. Smith, R. Chevalier, R. Schwartz, M. Dopita, and M. Shull for stimulating conversations and correspondence. This work was performed at the University of Wisconsin, was supported by the Department of Physics Fellowship and by NASA grant NGL 50-002-044, and was revised at the Center for Astrophysics under contract NAS 5-3949.

REFERENCES

Allen, C. W. 1973, *Astrophysical Quantities* (3d ed.; London: Athlone).
Bely, O., and Faucher, P. 1970, *Astr. Ap.*, **6**, 88.
Benson, R. S., and Kulander, J. L. 1972, *Solar Phys.*, **27**, 305.
Blaha, M. 1972, *Astr. Ap.*, **16**, 437.
Böhm, K. H., Siegmund, W. A., and Schwartz, R. D. 1976, *Ap. J.*, **203**, 399.
Brocklehurst, M. 1971, *M.N.R.A.S.*, **153**, 471.
Burgess, A., and Tworkowski, A. S. 1976, *Ap. J. (Letters)*, **205**, L105.
Burke, J. R., and Silk, J. 1974, *Ap. J.*, **190**, 1.
Cox, D. P. 1970, Ph.D. thesis, University of California, La Jolla.
———. 1972*a*, *Ap. J.*, **178**, 143.
———. 1972*b*, *Ap. J.*, **178**, 149.
Chevalier, R. A. 1974, *Ap. J.*, **188**, 501.
Chevalier, R. A., and Theys, J. C. 1975, *Ap. J.*, **195**, 53.
Daltabuit, E. 1972, Ph.D. thesis, University of Wisconsin, Madison.
Davis, J. 1974, *J. Quant. Spectrosc. Rad. Transf.*, **14**, 549.
deNoyer, L. K. 1974, *A.J.*, **79**, 1253.
Dopita, M. A. 1976, *Ap. J.*, **209**, 395.
———. 1977, *Ap. J. Suppl.*, **33**, 437.
———. 1978, *Ap. J. Suppl.*, **37**, 117.
Dufour, R. J. 1975, *Ap. J.*, **195**, 315.
Field, G. B., and Steigman, G. 1971, *Ap. J.*, **166**, 59.
Flower, D. R., and Launay, J. M. 1973, *Astr. Ap.*, **29**, 321.
Fry, M. A., and Aller, L. H. 1975, *Ap. J. Suppl.*, **29**, 55.
Jenkins, E. B., Silk, J., and Wallerstein, G. 1976, *Ap. J. Suppl.*, **32**, 681.
Johnston, W. D., III, and Kunze, H.-J. 1971, *Phys. Rev. A*, **4**, 962.
Jura, M. 1976, *Ap. J.*, **206**, 691.
Krueger, T. K., and Czyzak, S. J. 1970, *Proc. Roy. Soc. London, A*, **318**, 531.
MacAlpine, G. M. 1971, Ph.D. thesis, University of Wisconsin, Madison.
McCray, R., Stein, R. F., and Kafatos, M. 1975, *Ap. J.*, **196**, 565.
Mewe, R. 1972, *Astr. Ap.*, **20**, 215.
Miller, J. S. 1974, *Ap. J.*, **189**, 239.
Milne, D. K. 1968, *Australian J. Phys.*, **21**, 501.
Münch, G. 1977, *Ap. J. (Letters)*, **212**, L77.
Osterbrock, D. E. 1958, *Pub. A.S.P.*, **70**, 399.
Osterbrock, D. E., and Costero, R. 1973, *Ap. J. (Letters)*, **184**, L71.
Osterbrock, D. E., and Dufour, R. J. 1973, *Ap. J.*, **185**, 441.
Pengelly, R. M. 1963, *M.N.R.A.S.*, **127**, 145.
Pradhan, A. S. 1976, *M.N.R.A.S.*, **177**, 31.
Rappaport, S., Doxsey, R., Solinger, R. A., and Borken, R. 1974, *Ap. J.*, **194**, 329.
Raymond, J. C. 1976, Ph.D. thesis, University of Wisconsin, Madison.
Raymond, J. C., and Smith, B. W. 1977, *Ap. J. Suppl.*, **35**, 419.
Robb, D. M., and Garstang, G. H. 1975, private communication.
Robbins, R. R. 1968, *Ap. J.*, **151**, 497.
Robbins, R. R., and Robinson, E. L. 1971, *Ap. J.*, **167**, 249.
Roberts, D. E. 1970, *J. Phys. B*, **3**, 676.
Saraph, H. E., and Seaton, M. J. 1970, *M.N.R.A.S.*, **148**, 367.
Schwartz, R. D. 1975, *Ap. J.*, **195**, 631.
———. 1976, *Pub. A.S.P.*, **88**, 159.
———. 1977, preprint.
Shull, J. M., and McKee, C. F. 1978, preprint.
Silk, J., and Burke, J. R. 1974, *Ap. J.*, **190**, 11.
Spitzer, L., Jr., and Jenkins, E. B. 1975, *Ann. Rev. Astr. Ap.*, **13**, 133.
Steigman, G. 1975, *Ap. J.*, **199**, 642.
Strom, K. M., Strom, S. E., and Kinman, T. D. 1974, *Ap. J. (Letters)*, **191**, L93.

Tondello, G., and McWhirter, R. W. P. 1971, *J. Phys. B*, **4**, 715.
Tully, J. A., Petrini, D., and Bely, O. 1973, *Astron. & Astrophys.*, **23**, 15.
Wiese, W. L., Smith, M. W., and Glennon, B. M. 1966, NSRDS–NBS 4.
Wiese, W. L., Smith, M. W., and Miles, B. M. 1969, NSRDS–NBS 22.
Witt, A. N., and Johnson, M. W. 1973, *Ap. J.*, **181**, 363.
Woodgate, B. E., Stockman, H. S., Jr., Angel, J. R. P., and Kirshner, R. P. 1974, *Ap. J.* (*Letters*), **188**, L79.

JOHN C. RAYMOND: Harvard-Smithsonian Center for Astrophysics, 60 Garden Street, Cambridge, MA 02138